Cell

Article

Apocalmodulin Itself Promotes Ion Channel Opening and Ca^{2+} Regulation

Paul J. Adams,[1] Manu Ben-Johny,[1] Ivy E. Dick,[1] Takanari Inoue,[2,3] and David T. Yue[1,*]

[1]Calcium Signals Laboratory, Departments of Biomedical Engineering and Neuroscience, Center for Cell Dynamics, The Johns Hopkins University School of Medicine, 720 Rutland Avenue, Baltimore, MD 21205, USA

[2]Department of Cell Biology and Center for Cell Dynamics, The Johns Hopkins University School of Medicine, 855 N. Wolfe Street, Baltimore, MD 21205, USA

[3]Precursory Research for Embryonic Science and Technology, Japan Science and Technology Agency, 4-1-8 Honcho Kawaguchi, Saitama 332-0012, Japan

*Correspondence: dyue@jhmi.edu

http://dx.doi.org/10.1016/j.cell.2014.09.047

SUMMARY

The Ca^{2+}-free form of calmodulin (apoCaM) often appears inert, modulating target molecules only upon conversion to its Ca^{2+}-bound form. This schema has appeared to govern voltage-gated Ca^{2+} channels, where apoCaM has been considered a dormant Ca^{2+} sensor, associated with channels but awaiting the binding of Ca^{2+} ions before inhibiting channel opening to provide vital feedback inhibition. Using single-molecule measurements of channels and chemical dimerization to elevate apoCaM, we find that apoCaM binding on its own markedly upregulates opening, rivaling the strongest forms of modulation. Upon Ca^{2+} binding to this CaM, inhibition may simply reverse the initial upregulation. As RNA-edited and -spliced channel variants show different affinities for apoCaM, the apoCaM-dependent control mechanisms may underlie the functional diversity of these variants and explain an elongation of neuronal action potentials by apoCaM. More broadly, voltage-gated Na channels adopt this same modulatory principle. ApoCaM thus imparts potent and pervasive ion-channel regulation.

INTRODUCTION

Calmodulin (CaM) lacking bound Ca^{2+} (apocalmodulin, apoCaM) has often been categorized as less capable of modulating target molecules, compared to CaM loaded with Ca^{2+} (Ca^{2+}/CaM) (Alberts et al., 1994). Certainly, there have been exceptions to this premise (Jurado et al., 1999), but CaM regulation of ion channels has seemingly followed the traditional order (Saimi and Kung, 2002). This study argues to the contrary for voltage-gated Ca^{2+} and Na channels.

Among the most salient examples of CaM modulation are those involving L type ($Ca_V1.3$) Ca^{2+} channels. These transport molecules serve as a dominant Ca^{2+} entry pathway into pacemaking cardiomyocytes and neurons (Bean, 2007) and figure crucially in rhythmic functions like cardiac pacemaking and motor control involving substantia nigra, the prime neurodegenerative locus in Parkinson's (Chan et al., 2007; Obeso et al., 2008). As these channels convey substantial Ca^{2+} entry in these settings, modulation of $Ca_V1.3$ is critical for Ca^{2+} signaling and homeostasis in health and disease (Bean, 2007; Chan et al., 2007; Puopolo et al., 2007).

One better-studied form of $Ca_V1.3$ regulation is the Ca^{2+}-dependent inactivation (CDI) of this channel type by CaM (Evans and Zamponi, 2006). At first glance, the operation of CDI may now seem simple in coarse outline, at least for the best-studied $Ca_V1.3$ channel variant (Ben-Johny and Yue, 2014). This "archetypical" form is distinguished by an IQ CaM-binding domain containing the sequence isoleucine-glutamine-aspartate-tyrosine (IQDY), followed by a stop codon soon after (Figure 1A, variant 0). A single Ca^{2+}-free CaM molecule (apoCaM) first preassociates with sites including the IQ domain (Figure 1B, configuration *A*), thus becoming a resident, but presumably dormant, Ca^{2+} sensor poised for subsequent channel regulation (Bazzazi et al., 2013; Ben-Johny et al., 2013; Erickson et al., 2003; Liu et al., 2010; Pitt et al., 2001). Ca^{2+} binding to this onboard apoCaM then sharply reduces channel open probability (P_O) (Figure 1B, configuration *I*) (Ben-Johny et al., 2013), furnishing Ca^{2+}-negative feedback crucial for Ca^{2+} handling. Channels without apoCaM cannot undergo CDI (Bazzazi et al., 2013; Ben-Johny et al., 2013; Liu et al., 2010).

That said, the full reality of the modulatory landscape is staggering in its complexity, given recent discoveries of a prominent array of RNA-edited and splice variants of $Ca_V1.3$ (rest of Figure 1A). RNA editing yields different sequences in the IQ element (Huang et al., 2012), and alternative splicing produces channels with conspicuous extensions after the IQ domain (Bock et al., 2011; Hui et al., 1991; Tan et al., 2011; Xu and Lipscombe, 2001). These newly recognized variants actually constitute the bulk of $Ca_V1.3$ channels in the brain, and they exhibit vast differences in CDI (Bazzazi et al., 2013; Bock et al., 2011; Huang et al., 2012; Tan et al., 2011), projecting this diversity as an extensive but largely unexplored system for tuning Ca^{2+} dynamics. But CDI tuning may only foreshadow a larger mysterious effect—heterologous expression of $Ca_V1.3$ variants frequently exhibits sharply diminished current densities that seem too prominent to attribute to happenstance (Bazzazi et al., 2013; Bock et al., 2011; Huang et al., 2012; Tan et al., 2011). Could a major

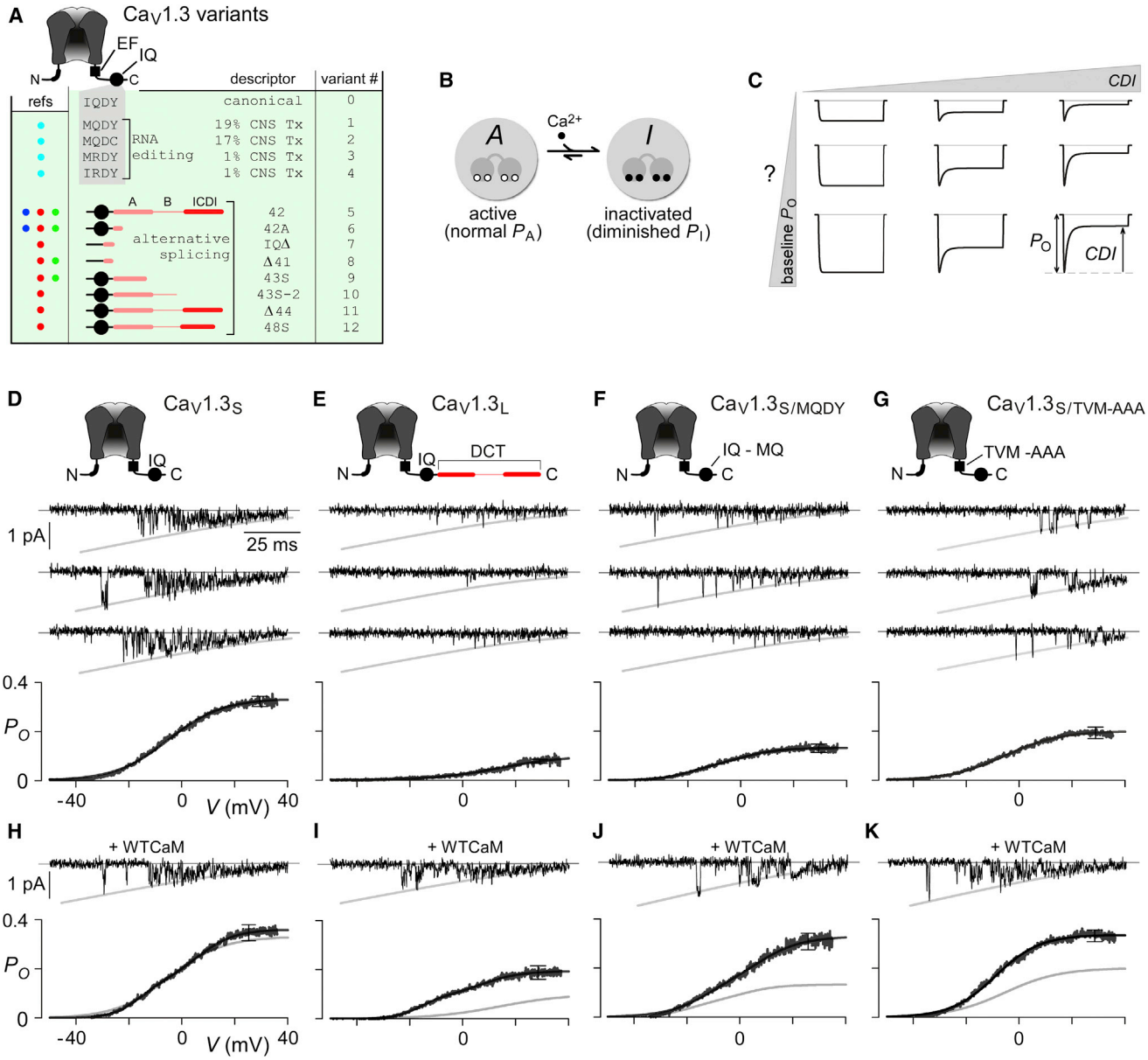

Figure 1. CaM Alters P_O of L Type Channel Variants at Single-Molecule Level

(A) $Ca_V1.3$ channel carboxy-tail variation by alternative splicing and RNA editing. Cyan, blue, red, and green symbols correspond, respectively, to references Huang et al., 2012; Hui et al., 1991; Tan et al., 2011; and Bock et al., 2011.

(B) Configuration *A* (active), channels (shown as gray circles) bound to apoCaM (shown as two lobes and linker) have high baseline P_O (P_A). Configuration *I* (inactivated), channels bound to Ca^{2+}-CaM have diminished channel P_O (P_I) (Ben-Johny et al., 2013; Imredy and Yue, 1994).

(C) Hypothetical fixed and idiosyncratic CDI and baseline P_O profiles for $Ca_V1.3$ variants.

(D–G) Single-channel analysis of four recombinant $Ca_V1.3$ variants transiently expressed in HEK293 cells with only endogenous CaM present. Top subpanels, unitary Ba^{2+} currents during voltage ramp, shown between −50 mV and +40 mV (slanted gray lines, GHK fit). Bottom subpanel, average single-channel P_O versus voltage.

(H–K) Single-channel records under elevated apoCaM. Light gray line reproduced from corresponding variant above.

All averages derived from multiple patches (n = 4–6). Error bars are ± SEM throughout. Behaviors shown for $Ca_V1.3_S$ (Extended Experimental Procedures for detailed sequence) in (A) and (D) were indistinguishable in this regard to those for a closely similar natural splice variant $Ca_V1.3_{42A}$ (Xu and Lipscombe, 2001) (not shown).

unsuspected action of $Ca_V1.3$ variation be to adjust baseline channel P_O, thereby producing an equally large or greater effect on Ca^{2+} signaling than CDI? Figure 1C cartoons the potential array of channel behaviors that would then result, where each hypothetical Ca^{2+} current trace portrays the functional profile of an individual variant. Whether such P_O effects actually exist across

variants and whether their mechanistic underpinnings relate to CDI remain open and difficult questions that cloud the physiology and pharmacological manipulation of $Ca_V1.3$ variant channels in relation to Ca^{2+} signaling and dysregulation.

Here, we exploit single-molecule and chemical-biological approaches to reveal a simple principle that may unify the spectrum of $Ca_V1.3$ molecular variants. In particular, we combine chemical-dimerizer-driven step increases in plasmalemmal CaM with simultaneous electrophysiological readouts of channel function (Luik et al., 2008; Spencer et al., 1993; Suh et al., 2006). We thus reveal that the binding of a single apoCaM to channels does considerably more than permit CDI to occur. ApoCaM binding itself also enhances channel opening (P_O) by several fold, rivaling the strongest forms of channel modulation (Miriyala et al., 2008). RNA editing, alternative splicing, and fluctuating CaM levels thus regulate CDI and baseline P_O, acting to variably populate pools of channels lacking or bound to apoCaM.

A key prediction is that elevated CaM should boost $Ca_V1.3$ opening and prolong neuronal action potentials. Indeed, we explicitly demonstrate this outcome in substantia nigral neurons. More broadly, a recent study reveals notable similarity between the Ca^{2+}/CaM regulation of Ca_V channels and that of voltage-gated Na_V channels (Ben-Johny et al., 2014). Here, we generalize this likeness, showing that apoCaM binding to Na_V channels also strongly amplifies P_O. Thus, apoCaM imparts a potent and pervasive form of ion-channel regulation, whose implications range as far as the sweep of Ca_V and Na_V superfamilies, and perhaps beyond (Saimi and Kung, 2002).

RESULTS

CaM Modulates Baseline Opening of L Type Channels

We first tested whether the baseline P_O of certain variant channels is in fact diminished, and whether CaM at all influences this P_O. Figure 1D displays the properties of the canonical $Ca_V1.3$ "short" splice variant ($Ca_V1.3_S$, Figure 1A, variant "0"), with the IQ domain translated as amino acids IQDY (as coded by genomic sequence). We used low-noise electrophysiology (Tay et al., 2012) to directly observe single-channel P_O and employed Ba^{2+} as the charge carrier through channels because Ba^{2+} binds poorly to CaM (Chao et al., 1984). This maneuver would thus preclude entry into configuration *I* (Figure 1B), allowing alterations in baseline P_O to be observed apart from CDI. Accordingly, a slow voltage ramp (shown from −50 to +40 mV) elicits stochastic openings that reflect near steady-state P_O at each voltage. The top rows display stochastic records, where channel closures correspond to the zero-current portions of the trace (on horizontal gray lines) and openings to downward deflections to the open level (slanted gray curves). Averaging many records yields a mean current that can be divided into the open level (slanted gray curve) to furnish the P_O versus voltage relation (sigmoidal trace at bottom), averaged over multiple patches.

Thus apprised, we examined the single-molecule properties of a prominently expressed $Ca_V1.3$ "long" splice variant (variant 5 in Figure 1A), featuring an extended distal carboxyl tail (DCT) as schematized atop Figure 1E. For convenience, we will refer to this variant as $Ca_V1.3_L$. Scrutiny of the single-trial records and P_O-*V* relation for this variant indeed reveals a far lower P_O. Interestingly, the presence of a DCT is not required for a diminished P_O because Figure 1F shows that a common RNA-edited variant within a short-splice configuration (variant 1 in Figure 1A, or $Ca_V1.3_{S/MQDY}$) also displays attenuated P_O compared to the canonical $Ca_V1.3_S$. Curiously, both $Ca_V1.3_L$ and $Ca_V1.3_{S/MQDY}$ exhibit diminished apoCaM binding affinity (Bazzazi et al., 2013; Liu et al., 2010). Thus, we tested for P_O effects in a man-made variant, where apoCaM affinity has been attenuated by mutations in the carboxyl tail of $Ca_V1.3_S$ ($Ca_V1.3_{S/TVM\text{-}AAA}$, cartooned atop Figure 1G) (Ben-Johny et al., 2013). $Ca_V1.3_{S/TVM\text{-}AAA}$ also exhibits reduced P_O (Figure 1G).

Given this pattern, we tested more directly for the involvement of apoCaM in modulating P_O, by strongly overexpressing recombinant CaM with these same constructs. Perhaps, P_O might be upregulated by apoCaM occupancy of some site, so that overexpressing CaM may boost occupancy by mass action. For the prototypic short variant $Ca_V1.3_S$, no such enhancement of P_O is produced by CaM overexpression (Figure 1H), as if the hypothetical site were already bound to CaM at baseline. By contrast, elevated CaM produces an impressive increase of P_O in all other constructs with diminished apoCaM affinity (Figures 1I–1K), where an appreciable fraction of channels might initially lack indwelling CaM.

Single-Channel P_O Modulated in Quantized Manner

However, overexpressing recombinant CaM could enhance channel P_O by a multitude of mechanisms besides binding to a channel modulatory site. For example, CaM-dependent modulation of various kinases and phosphatases or even gene regulation of auxiliary factors could be in play (Bers and Grandi, 2009). To garner further mechanistic constraints, we considered a distinctive feature of an apoCaM-binding model, as diagrammed atop Figure 2A. Here, beyond the configuration *A* described earlier, we explicitly hypothesize a configuration lacking apoCaM at a P_O modulatory site (configuration *E*). In this formulation, channels bound to apoCaM (configuration *A*) would open with a high P_O as exemplified by $Ca_V1.3_S$ (Figure 1D), and those lacking apoCaM would exhibit low P_O. A hallmark feature of this paradigm is that channel P_O should be quantized, manifesting as a high P_O "mode of channel gating" when apoCaM is bound (Hess et al., 1984) or a low P_O mode when apoCaM is absent. By contrast, many other mechanisms (e.g., multiple phosphorylation sites) could produce a graded spectrum of intermediate effects. These contrasts might be abundantly clear at the single-channel level.

Figure 2A displays twelve sequential single-channel trials of the RNA-editing variant $Ca_V1.3_{S/MQDY}$ with only endogenous CaM present. Activity was evoked by voltage ramps introduced at 12 s intervals. The activity appears uniformly sparse, as confirmed by the diary plot of average P_O within individual trials ($\bar{P}_O$, Figure 2B), as well as the single bell-shaped distribution of $\bar{P}_O$ drawn from a larger set of trials (Figure 2D). These results are consistent with a channel residing almost exclusively within a hypothesized configuration *E*. The corresponding average P_O-*V* relation (Figure 2C) may thus pertain to channels residing in configuration *E* alone.

By contrast, upon strongly coexpressing recombinant CaM with another $Ca_V1.3_{S/MQDY}$ channel (Figures 2E–2H), activity is

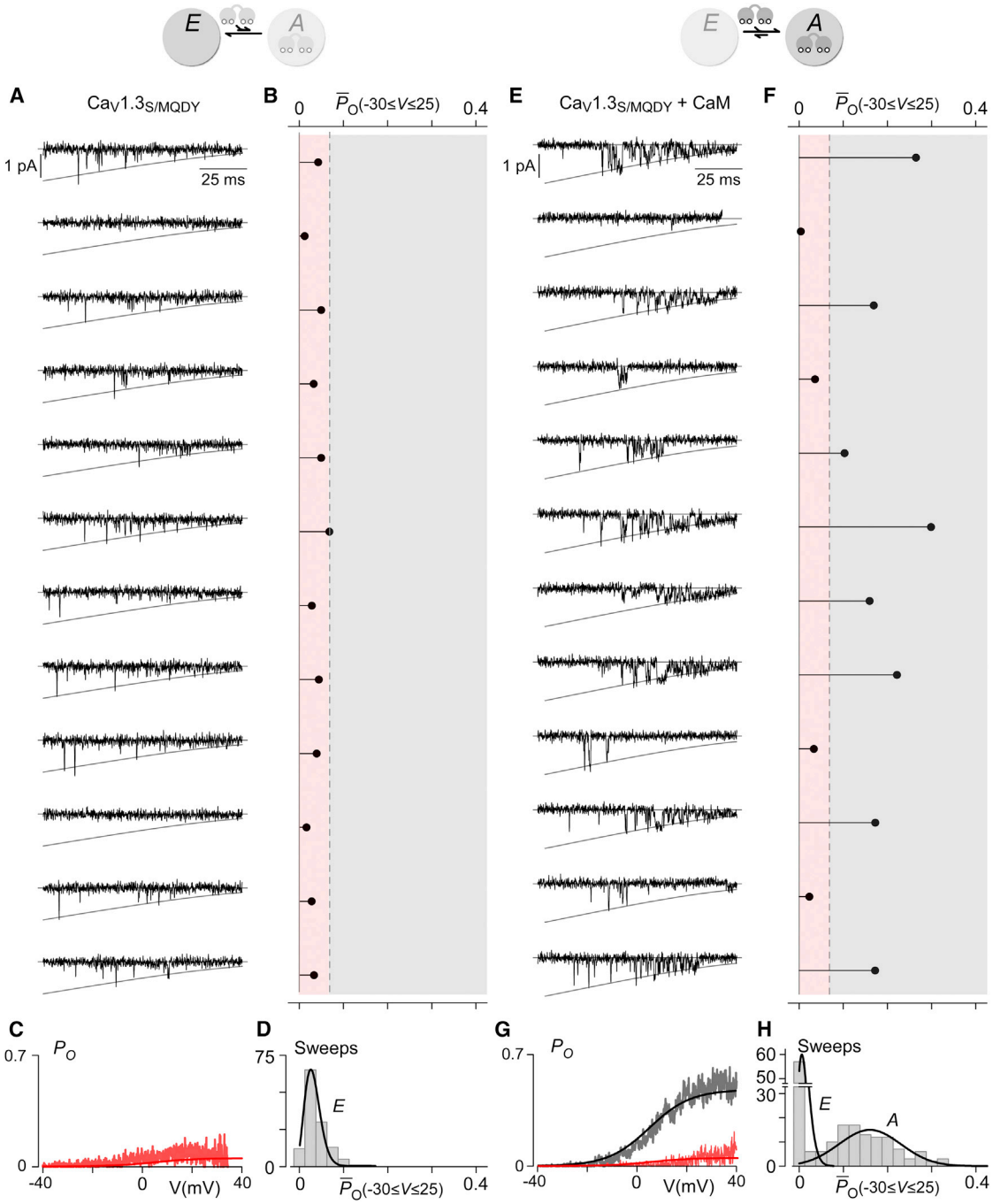

Figure 2. Single-Channel P_O Modulated by CaM in Quantized Manner

(A) $Ca_V1.3_{S/MQDY}$ in HEK cells with only endogenous CaM present; mainly expected to occupy configuration *E* (top cartoon). Single-channel Ba^{2+} currents during voltage ramp, shown between −40 and +40 mV, elicited at 12 s intervals.

(B) For each current trace in (A), average P_O between −30 and +25 mV ($\overline{P}_O$ ($-30 \leq V \leq 25$)) was calculated. Traces categorized into low P_O (red-shaded) region or high P_O range (gray-shaded).

(C) Average P_O at each voltage, calculated separately for traces in low P_O (red) versus high P_O range (gray). In this case, all traces are in low P_O group (red).

(D) Number of sweeps with $\overline{P}_O$ ($-30 \leq V \leq 25$) within indicated P_O ranges. Histogram fits with unimodal distribution ($p > 0.9$) by Hartigan's dip test (Extended Experimental Procedures).

(E–H) Same analysis for $Ca_V1.3_{S/MQDY}$ with CaM overexpression. (H) $\overline{P}_O$ histogram unlikely to be unimodal ($p < 0.05$, Hartigan's dip test), thus fit by bimodal distribution.

See also Figures S1 and S2.

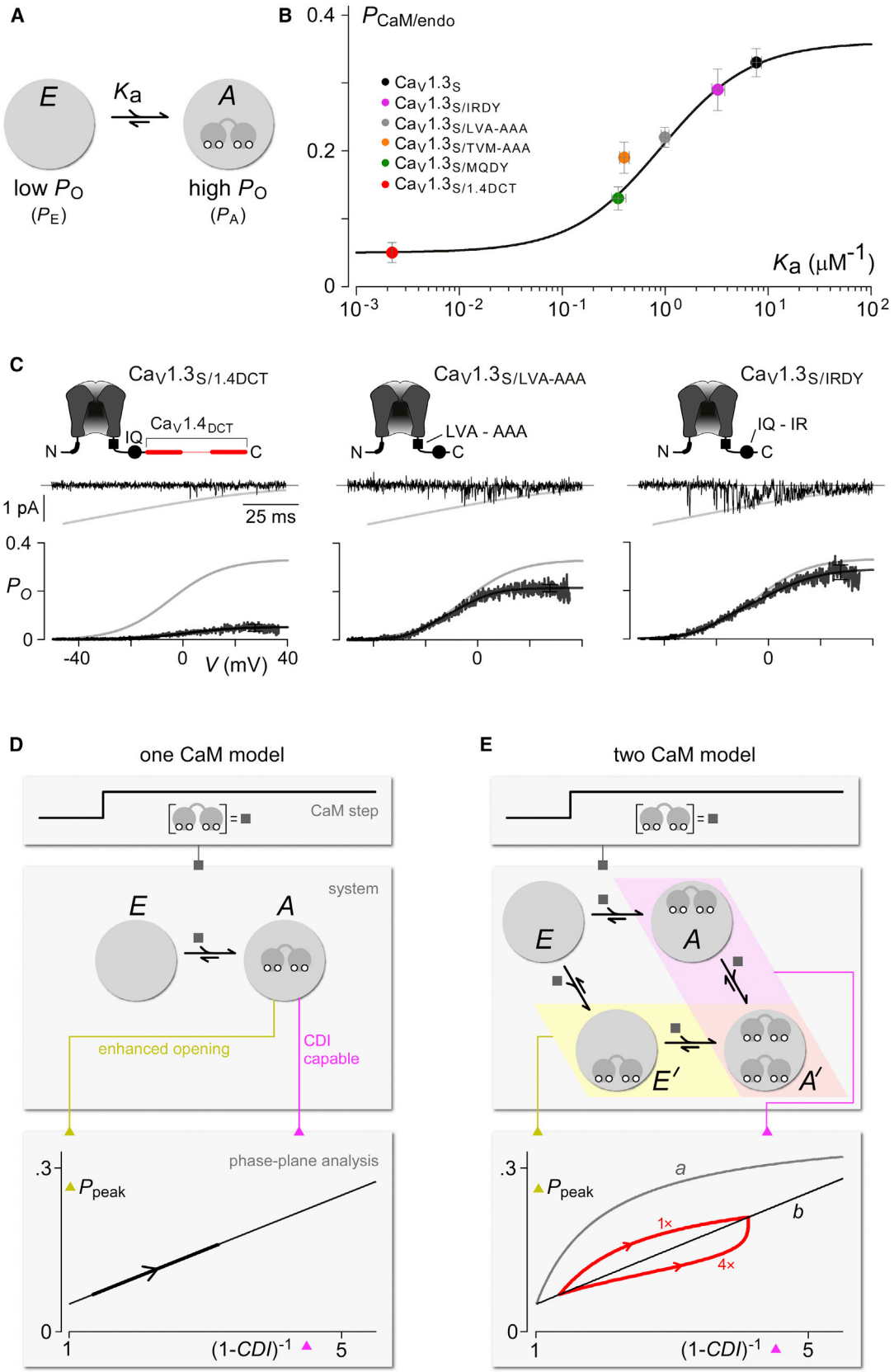

(legend on next page)

markedly enhanced in a conspicuously quantized manner. Although many trials exhibit a high P_O pattern of gating (Figure 2E, trials 1, 3, 5–8, 10, 12), low P_O trials resembling those without apoCaM overexpression (Figure 2A) are clearly interspersed (Figure 2E, trials 2, 4, 9, 11). This apparent quantization of high and low P_O gating is confirmed by the segregation of $\overline{P}_O$ into distinct zones in the diary plot (Figure 2F) and by the bimodal distribution of $\overline{P}_O$ amassed from a large number of trials (Figure 2H). Little intermediate activity can be discerned. These data are thus consistent with channel switching between discrete *E* and *A* configurations. By grouping trials into high and low P_O groups with the dashed-line discriminator in Figure 2F, we could estimate separate P_O-*V* relations for each gating mode (Figure 2G). Notably, the low P_O-*V* relation (red) is fit by the same function used without elevating apoCaM (Figure 2C), arguing for the invariance of configuration *E* between conditions. Also notable is the ~7-fold enhancement of high versus low P_O-*V* relations, suggesting an enormous effect of apoCaM on channel opening. Parallel experiments with other $Ca_V1.3$ variant channels ($Ca_V1.3_S$, $Ca_V1.3_L$, $Ca_V1.3_{S/TVM\text{-}AAA}$) confirmed similar quantized behavior (Figures S1 and S2).

ApoCaM Binding to CDI Site Correlates with Enhanced Baseline P_O

The digital manner by which apoCaM enhances baseline P_O fits well with a simple apoCaM-binding mechanism (top of Figure 2). Nonetheless, other plausible mechanisms could also elaborate quantized behavior, such as phosphorylation and dephosphorylation at a single site. To begin to discriminate among these possibilities, we noted that a direct CaM-binding mechanism for P_O modulation (Figure 3A) would predict a simple Langmuir relation between the peak P_O measured with only endogenous apoCaM present ($P_{CaM/endo}$) and the association constant for apoCaM binding to a presumed P_O modulatory site (K_a). Figure S3 yields:

$$P_{CaM/endo} = P_E + (P_A - P_E) \cdot K_a / (K_a + \Lambda) \quad (1)$$

where P_E is the open probability of channels lacking apoCaM (Figure 3A, configuration *E*), P_A the open probability of channels prebound to apoCaM (configuration *A*), and $\Lambda \propto [\text{apoCaM}_{bulk}]^{-1}$.

The challenge with applying tests based on this equation was the unknown identity of the hypothetical apoCaM-binding site for P_O modulation, much less the corresponding K_a for various $Ca_V1.3$ variants. Indeed, atomic structures of Ca^{2+}/CaM complexed with carboxy-tail peptides of closely related $Ca_V1.2$ channels argue for the binding of multiple CaM molecules per tail, each bound CaM imparting a different function (Fallon et al., 2009; Kim et al., 2010). That said, we conjectured that the apoCaM-binding site for P_O modulation might be one and the same as the site involved in the CDI process (Figure 1B). Elsewhere, we have previously determined the K_a values for apoCaM binding to the carboxy-tail site relating to CDI, not only for the $Ca_V1.3$ variants in Figures 1E–1H but also for additional variants whose P_O profiles are characterized in Figure 3C (Bazzazi et al., 2013; Ben-Johny et al., 2013; Liu et al., 2010). Plotting $P_{CaM/endo}$ versus K_a for all of these variants in Figure 3B then tests for the prediction of Equation 1. It is noteworthy how well the data symbols fit with the Langmuir function (smooth curve) in Figure 3B, an outcome consistent with the binding of one and the same apoCaM modulating both P_O and the ability to undergo CDI. For robustness, open probabilities were measured at maximal depolarization for the plot in Figure 3B.

Rapid Plasmalemmal Recruitment of ApoCaM Triggers Dual Modulation of P_O and CDI

Nonetheless, the suggestive correlation in Figure 3B requires compilation of data from several variants, characterized over multiple cells by differing techniques. By contrast, a considerably more direct test would arise if we could abruptly change the free apoCaM concentration at the cytoplasmic face of channels, all while performing electrophysiology within individual cells. The result would be revealing because the evolving values of CDI and P_O thus observed would adhere to a specific moment-to-moment interrelation if the one-apoCaM mechanism conjectured above were to hold true. This can be seen as follows in Figure 3D. The top subpanel portrays a hypothetical step-like increase in the free apoCaM concentration facing channels. This "input" would drive a scheme in which channel binding to a single apoCaM imparts a shift from configurations *E* to *A*, defined such that channels in *E* are incapable of undergoing CDI and exhibit a low P_O (P_E), whereas those in *A* demonstrate a robust CDI and a high P_O (P_A) before undergoing CDI. The following linear relation must then hold for a mixed population of channels, such as observed in whole-cell recordings (Figure S4),

$$I_{peak}/I_{max} = P_E \cdot (1 - CDI)^{-1}, \quad (2)$$

where I_{peak} is the peak Ca^{2+} current before CDI onset; I_{max} is the current amplitude if all channels in a cell were simultaneously open; *CDI* is the CDI metric defined in Figure 1C; and P_E is the open probability of channels in configuration *E* (= 0.051 from Figure 3C). In this relation, $(1-CDI)^{-1}$ may be considered a linearized CDI metric, starting at one when *CDI* is absent, and growing larger as *CDI* intensifies. As well, I_{peak} / I_{max} turns out to be the average peak open probability of all channels in a cell before CDI onset, referred to as P_{peak}. That said, the thin black line in

Figure 3. ApoCaM Affinity Tunes P_O

(A) Proposal that channel apoCaM affinity (K_a) specifies equilibrium between configurations *E* (low P_O) and *A* (high P_O).

(B) Plot of peak P_O obtained with only endogenous CaM present ($P_{CaM/endo}$) versus previously estimated association constants gauged by live-cell FRET between channel carboxyl termini and apoCaM (Figure S3 and Table S1). Error bars are ± SEM.

(C) Average P_O (format as in Figures 1E–1L) for recombinant $Ca_V1.3_S$ channels with variant carboxyl tails yielding reduced apoCaM affinity. Gray lines from basic $Ca_V1.3_S$ (Figure 1E) for comparison. All averages from multiple patches (n = 3–6). Error bars are ± SEM.

(D) Phase-plane signature of single-CaM behavior during CaM transients.

(E) Two-CaM behavior during CaM transients, revealed by phase-plane paradigm.

See also Figure S4.

the bottom subpanel of Figure 3D explicitly plots Equation 2. Here, a key feature concerns the immutable interrelation between P_{peak} and $(1-CDI)^{-1}$, even during an abrupt increase of apoCaM. Even though apoCaM binding to channels would deviate from equilibrium during such a transition, all P_{peak} versus $(1-CDI)^{-1}$ points would nonetheless reside on the same line (thick black arrow trajectory). This feature arises because each point on the trajectory corresponds to a specific fraction of channels bound to apoCaM, and each fraction enforces a unique pairing of P_{peak} versus $(1-CDI)^{-1}$ values. In this scheme, then, there are no arrangements that fall outside this regime.

By contrast, if the enhancement of baseline P_O were governed by a separate process other than the apoCaM binding that arms channels for CDI, deviation from the linear relation in Figure 3D would likely occur. For concreteness, consider a system where apoCaM binding to one site enables CDI to proceed (Figure 3E, middle subpanel, configurations within magenta zone), but apoCaM binding to an alternative site (yielding configurations in yellow zone) increases baseline P_O before CDI onset, from P_E to P_A. For simplicity, apoCaM binding to these sites is assumed to occur independently, and the steady-state fraction of peak current remaining after CDI is set to reproduce the experimentally observed CDI in $Ca_V1.3_S$ (Ben-Johny et al., 2013). If the dissociation constants for apoCaM binding to P_O ($K_{d|P}$) and CDI ($K_{d|CDI}$) sites were equivalent, then the two-CaM scheme would predict the downwardly convex relation between P_{peak} and $(1-CDI)^{-1}$ (Figure 3E, curve *a* in bottom subpanel), contrasting with the linear relation for the one-CaM scheme. However, if $K_{d|CDI}$ were precisely equal to $K_{d|P} \cdot P_E / P_A$, then the two-CaM scheme would still enforce the linear relation in the bottom subpanel of Figure 3E (curve *b*) at steady state, where this line would be identical to that for the one-CaM scheme (Figure S4). However, even here, the difference in dissociation constants at the two sites means that the transient response to abrupt changes in apoCaM would deviate from the linear steady-state relation; this outcome is demonstrated by the numerically simulated hysteretic trajectories in Figure 3E (red), where the *CDI* regulatory site loads at the same rate or faster than the P_O site as marked (Figure S4). In sum, this manner of analysis relating to abrupt changes in apoCaM furnishes powerful means to distinguish among differing mechanisms. Likewise, other potential P_O modulatory mechanisms, like channel phosphorylation, would predict analogous deviations from linearity (Equation 2), particularly during abrupt increases in apoCaM.

We therefore exploited chemical-biological step generation of apoCaM concentration at the cytoplasmic face of channels, based on rapamycin-triggered dimerization of cytoplasmic FK506-binding protein (FKBP) and the FKBP-rapamycin-binding protein (FRB) localized to plasmalemma by a signal sequence from Lyn kinase (Lyn-FRB) (Phua et al., 2012). Figure 4A cartoons the layout, where bath-applied rapamycin should sharply increase perimembranous apoCaM, as confirmed by confocal microscopy visualizing the FKBP–CaM moiety (Figure 4B, top). Line-histogram analysis reveals a 6-fold increase of perimembranous CaM with $\tau \sim 20$ s (Suh et al., 2006) (Figure 4B, bottom). Hence, coexpressing $Ca_V1.3$ variants in this context would permit electrophysiological readouts of P_O and CDI during periods of rapidly increasing apoCaM.

$Ca_V1.3_S$ serves as a control (Figure 4C). Because of its high apoCaM affinity at the CDI site, most channels here might already be charged with apoCaM at baseline, such that increasing apoCaM with rapamycin should produce negligible change. The top two rows display diary plots of peak current and CDI measured from Ca^{2+} currents evoked every 20 s by 30 mV step depolarizations, with corresponding current waveforms shown below. The baseline P_O of channels is proportional to peak current, which is displayed in a normalized format (I_{peak} / I_O, as defined below) to facilitate averaging across cells. The metric of CDI (*CDI*) is specified by I_Δ / I_{peak}, with these measures also diagrammed below. As expected, augmentation of apoCaM concentration by rapamycin negligibly perturbed either metric.

By contrast, for an RNA-edited variant ($Ca_V1.3_{S/MQDY}$) with moderate apoCaM affinity, a markedly different outcome arises (Figure 4D). Here, rapamycin-induced CaM enrichment causes a hand-in-hand increase of peak current and CDI, clearly evident in exemplar traces on the bottom. These trends are entirely corroborated by averaged diary plots above (green circles, top and middle rows). Similarly, parallel increases in peak current and CDI were observed for two other variants featuring reduced aggregate apoCaM affinity (Figures 4E and 4F), each with distinctive response kinetics to the step increase of apoCaM. As a control, parallel experiments performed without CaM fused to FKBP invariably showed no changes in either peak current or CDI upon application of rapamycin, verifying that the observed effects were due to CaM enrichment and not FKBP itself (Figure S5). Also, current densities for variants predicted to lack apoCaM at baseline (Figures 4D–4F) were on average smaller than for $Ca_V1.3_S$ (Figure 4C), as would be expected if P_O were diminished without bound apoCaM (Figure S5E). Finally, recruiting a CaM mutant unable to bind Ca^{2+} (CaM_{1234}), and using Ba^{2+} as the charge carrier, provided further evidence that apoCaM is in fact responsible for the observed enhancement in P_O (Figure S6).

One CaM Augments Baseline P_O and Enables CDI

With these well-behaved transient responses in hand, we undertook mechanistic analysis relating to moment-to-moment plots of P_{peak} versus $(1-CDI)^{-1}$. Figure 5A renders as dark green symbols the data from the exemplar cell in Figure 4D ($Ca_V1.3_{S/MQDY}$), with explicit labeling of points (i, ii, and iii) corresponding to exemplar currents shown earlier. The only free parameter is I_{max} in Equation 2, which was adjusted only to vertically normalize the data. Accordingly, the observed linearity and correspondence to predicted slope P_E is intrinsic to the data set. Therefore, adherence of these data points, and those from additional cells (pale green symbols), to the one-CaM relation throughout the CaM step is significant. Applying the same analysis to data from the exemplar cell in Figure 4E ($Ca_V1.3_L$) also demonstrates strict conformity to the same linear relation, even with numerous points drawn from the transient phase of the response (Figure 5B, dark blue symbols). Points from other cells (pale blue symbols) also adhere nicely to the same relation. Data for the exemplar cell relating to still another variant (Figure 4F, $Ca_V1.3_{S/1.4DCT}$) also reside on the same line (Figure 5C, dark red symbols), and additional cells also conformed to the same line (pale red symbols). Finally, Figure 5D overlays all these

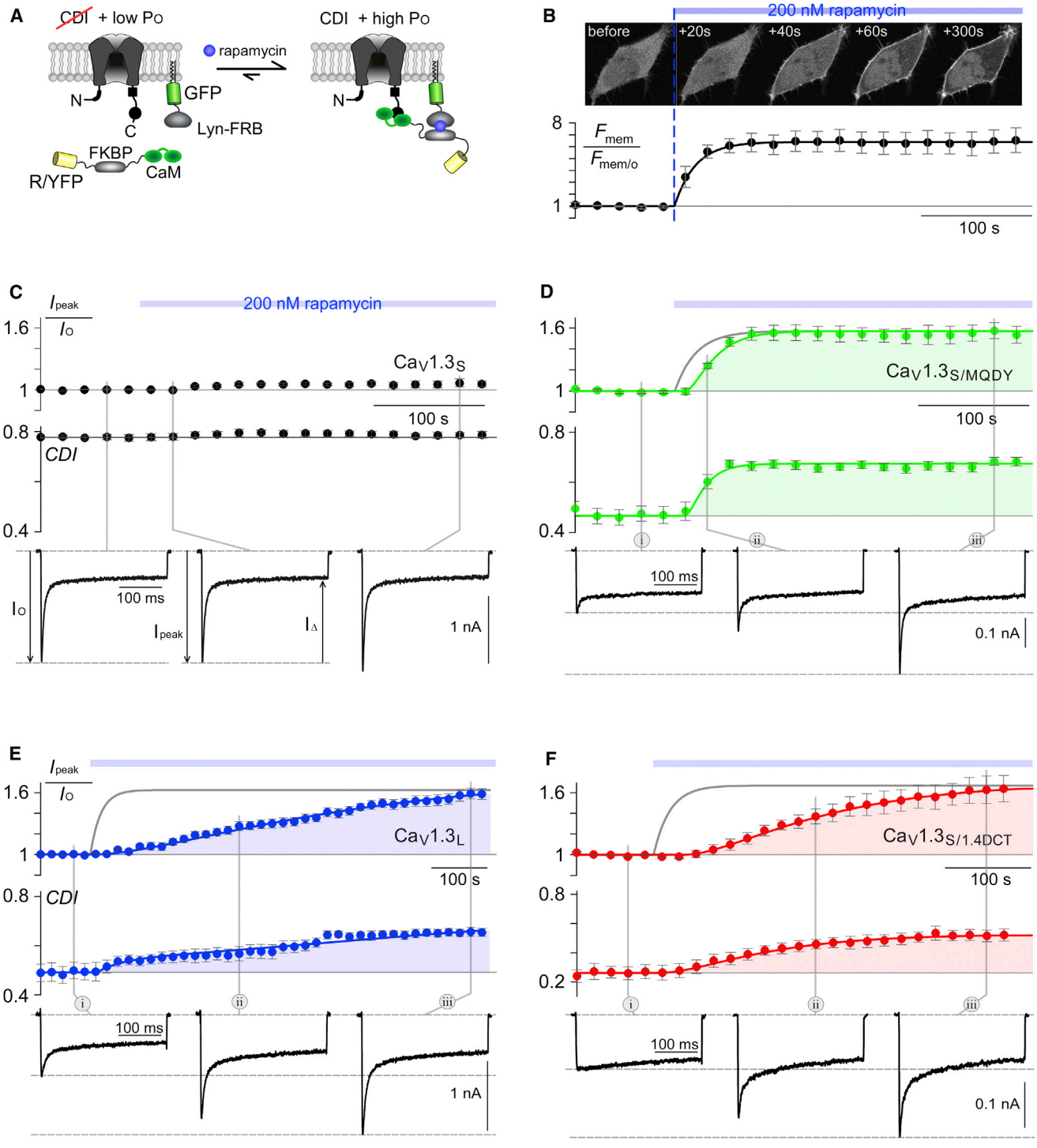

Figure 4. Step Increases in CaM Rapidly Modulate Both Peak Current and CDI

(A) Recombinant channels in HEK293 cells with both membrane-localized GFP-tagged FRB and cytosolic RFP/YFP-tagged FKBP fused to wild-type CaM.

(B) Top, confocal image of RFP/FKBP/CaM translocation to plasma membrane on 200 nM rapamycin perfusion. Bottom, time course of RFP membrane fraction measured every 20 s (n = 7 cells).

(C) Diary of normalized peak current (top subpanel) and CDI (middle subpanel) from whole-cell Ca^{2+} currents through $Ca_V1.3_S$ channels, evoked at 20 s intervals by steps to +30 mV from −90 mV holding potential. Corresponding current waveforms below.

(D–F) Normalized peak current and CDI for $Ca_V1.3$ variants with reduced apoCaM affinity. Format as in (C). Gray fit of apoCaM recruitment to plasmalemma from (B). All peak current and CDI measures obtained from multiple cells (n = 4–8). Error bars are ± SEM in (B)–(F). See also Figures S5 and S6.

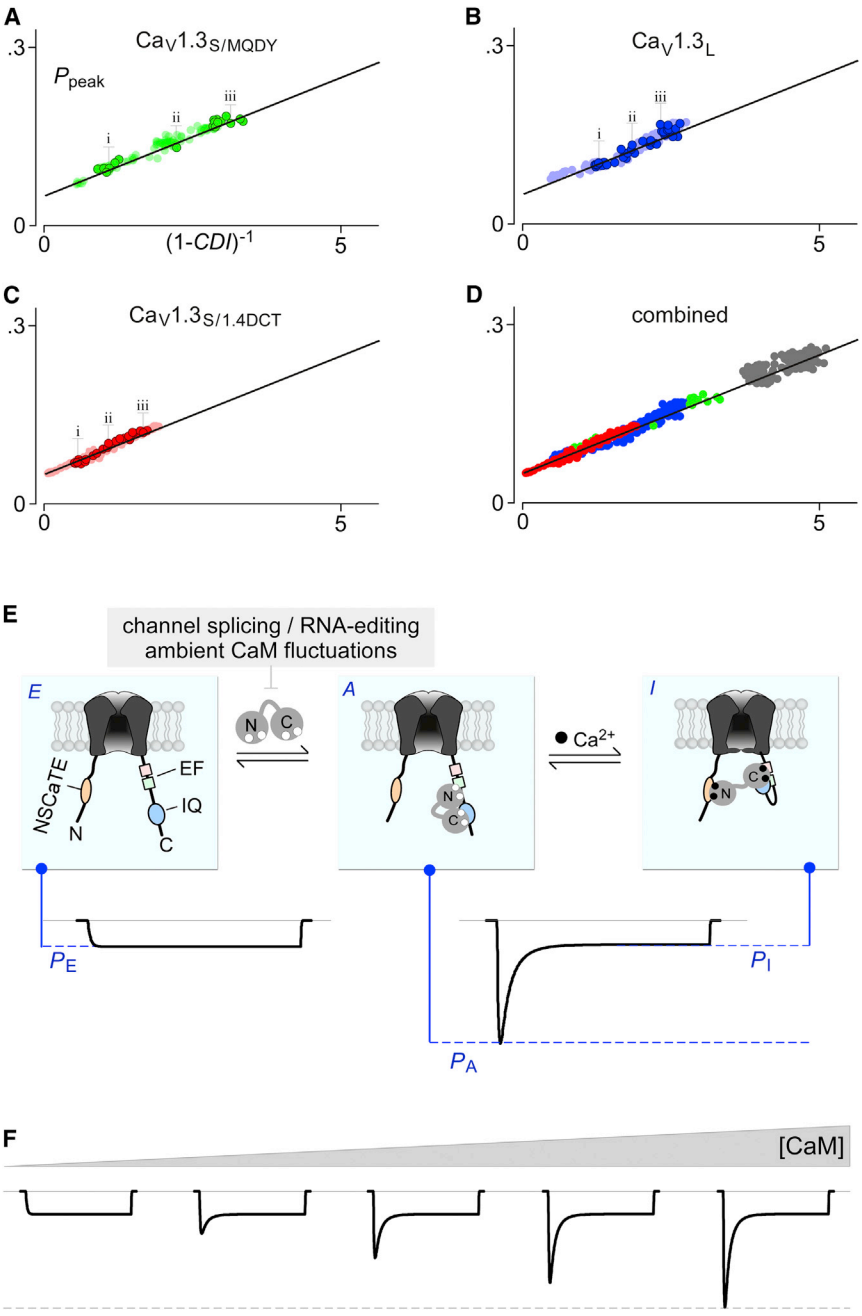

Figure 5. Phase-Plane Analysis Indicates that One CaM Modulates Both P_O and CDI

(A) Dark green symbols for exemplar cell in Figure 4D ($Ca_V1.3_{S/MQDY}$), with labeled points (i, ii, and iii) corresponding to exemplar currents in Figure 4D. Pale green symbols, data from additional cells expressing $Ca_V1.3_{S/MQDY}$.

(B and C) Same analysis for exemplar cells in Figure 4E ($Ca_V1.3_L$, dark blue symbols) and Figure 4F ($Ca_V1.3_{S/1.4DCT}$, dark red symbols), respectively. Pale symbols, data from additional cells.

(D) Data from additional cells for each variant and for a further canonical $Ca_V1.3_S$ variant (dark gray symbols) (n = 23 cells).

(E) One-apoCaM mechanism unifies diversity of baseline P_O and CDI properties of $Ca_V1.3$ variants.

(F) Simulation of P_O–CDI coordination with free apoCaM concentration for a single $Ca_V1.3$ variant.

data, and those of another variant (gray symbols, $Ca_V1.3_S$), thus arguing strongly for compliance with a single linear relation. On this basis, we propose the simple one-apoCaM mechanism in Figure 5E, which may unify the diversity of baseline P_O and CDI properties of numerous variants (Figure 1A). RNA-editing and splice variants modulate P_O and CDI over a large range, largely by tuning the affinity of apoCaM binding to channels (in configuration *E*), rather than by specialized molecular mechanisms particular to each variant. Fluctuations in ambient apoCaM could also tune $Ca_V1.3$ as shown in Figure 5F. Two realms of generalization immediately follow.

Predicted Neuronal Action Potential Elongation

The strong upregulation of $Ca_V1.3$ channel P_O by apoCaM promises significant consequences, particularly where $Ca_V1.3$ channels contribute prominently to pacemaking, such as in the substantia nigral neurons modulating movement control (Chan et al., 2007; Christel et al., 2012; Obeso et al., 2008). Importantly, elevated Ca^{2+} in dopaminergic neurons in the substantia nigra pars compacta (SNc) predisposes for neurodegeneration in Parkinson's disease (Bezprozvanny, 2009). $Ca_V1.3$ channels here support the bulk of Ca^{2+} entry (Bean, 2007; Cardozo and Bean, 1995; Chan et al., 2007; Puopolo et al., 2007), and Ca^{2+} channel activity shapes action potential (AP) morphology (Nedergaard, 1999; Puopolo et al., 2007). These neurons express a variety of $Ca_V1.3$ splice and RNA-edited variants as shown in Figure 1A (Bock et al., 2011; Huang et al., 2012), and elevating CaM in these cells drives CaM onto low-affinity channel variants by mass action (Bazzazi et al., 2013). Numerical simulations described below predict that apoCaM enhancement of $Ca_V1.3$ opening should produce telling changes in action-potential morphology, which we tested for experimentally as follows.

SNc dopaminergic neurons were dissected from transgenic mice selectively expressing GFP under the tyrosine hydroxylase (TH) promoter, enabling robust identification via fluorescence (Figure 6A, left subpanel). After culture for 1–7 days, cells maintained typical autonomous pacing at 1.0 ± 0.03 Hz (middle subpanel) and AP morphology (right subpanel) (Chan et al., 2007; Grace and Bunney, 1984; Puopolo et al., 2007). The AP duration at 90% of baseline (APD_{90}) was 7.4 ± 0.03 ms, as expected from

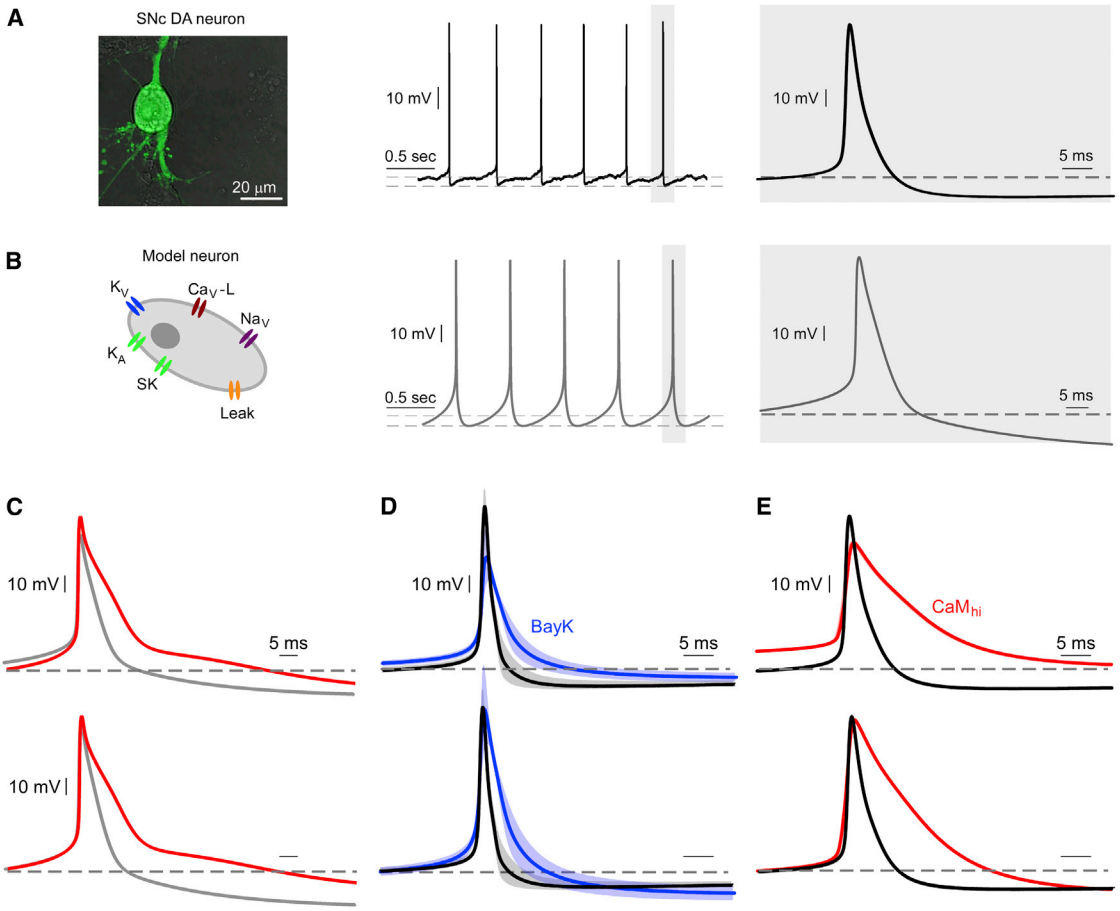

Figure 6. Predicted AP Elongation in Neurons

(A) Confocal image of cultured mouse substantia nigra (pars compacta) dopamine neuron (left subpanel). Middle subpanel, representative current-clamp recording of pacing in a SNc DA neuron in culture. Right subpanel, characteristic AP waveform obtained by averaging ~2,100 APs.

(B) Quantitative in silico model (left subpanel). Numerical simulations of pacing (middle subpanel) and AP morphology (right subpanel) are shown.

(C) Simulated AP waveforms with fraction of $Ca_V1.3$ channels bound to apoCaM equal to 0.3 (gray), compared to fraction bound of unity (red). Top subpanel, raw waveforms; bottom subpanel, normalized waveforms. See Extended Experimental Procedures and Table S2.

(D) Average AP from cultured SNc DA neurons before (black trace), and after applying Bay K8644 (5 μM) (blue trace) (n > 620 APs).

(E) AP recorded in SNc DA neurons with only endogenous CaM present (black trace) and with CaM overexpression (red trace) (n > 800 APs).

All APs measured from n = 4–5 cells. SEM shown as shading in (D) and (E).

prior reports (Puopolo et al., 2007). To predict the effects of apoCaM-driven P_O enhancement on AP morphology, we performed in silico simulations with a model (Chan et al., 2007) that closely recapitulated the firing pattern and AP morphology of these cultured neurons (Figure 6B) (Extended Experimental Procedures). Upon increasing the fraction of $Ca_V1.3$ channels bound to CaM by 3-fold, simulated AP waveforms elongate dramatically from the gray baseline trace to the red waveform (Figure 6C). The top subpanel displays raw waveforms, and the bottom subpanel normalizes these responses to facilitate visual comparison of durations. Current-clamp records in cultured neurons confirmed that enhancement of L type channel P_O by Bay K8644 induced similar AP prolongation, with APD_{90} increasing from 4.9 ± 0.92 to 11.5 ± 1.55 ms (Figure 6D). The key test came with lentiviral-mediated overexpression of wild-type CaM, yielding a striking increase of APD_{90} from 7.4 ± 0.03 ms with endogenous CaM to 24.3 ± 0.40 ms on overexpressing CaM (Figure 6E). Thus, fluctuations of apoCaM could alter AP morphology in substantia nigra and elsewhere in the brain (Bazzazi et al., 2013).

ApoCaM P_O Modulation Extends to Na_V Channels

The marked apoCaM modulation of $Ca_V1.3$ gave reason to wonder whether this scheme might generalize to other ion channels. In particular, voltage-gated Na channels (Na_V) have recently been shown to exhibit CaM-mediated CDI that appears remarkably similar to that in Ca_V channels (Ben-Johny et al., 2014). Moreover, earlier experiments report that apoCaM binds the carboxyl tail of Na_V channels (Herzog et al., 2003), an interaction confirmed in Figure S7. Given the extensive role of Na_V channels in fast electrical conduction within brain, heart, and muscle (Hille, 1984), we tested for apoCaM modulatory effects in Na_V channels. As alanine substitutions in the IQ domain of skeletal muscle

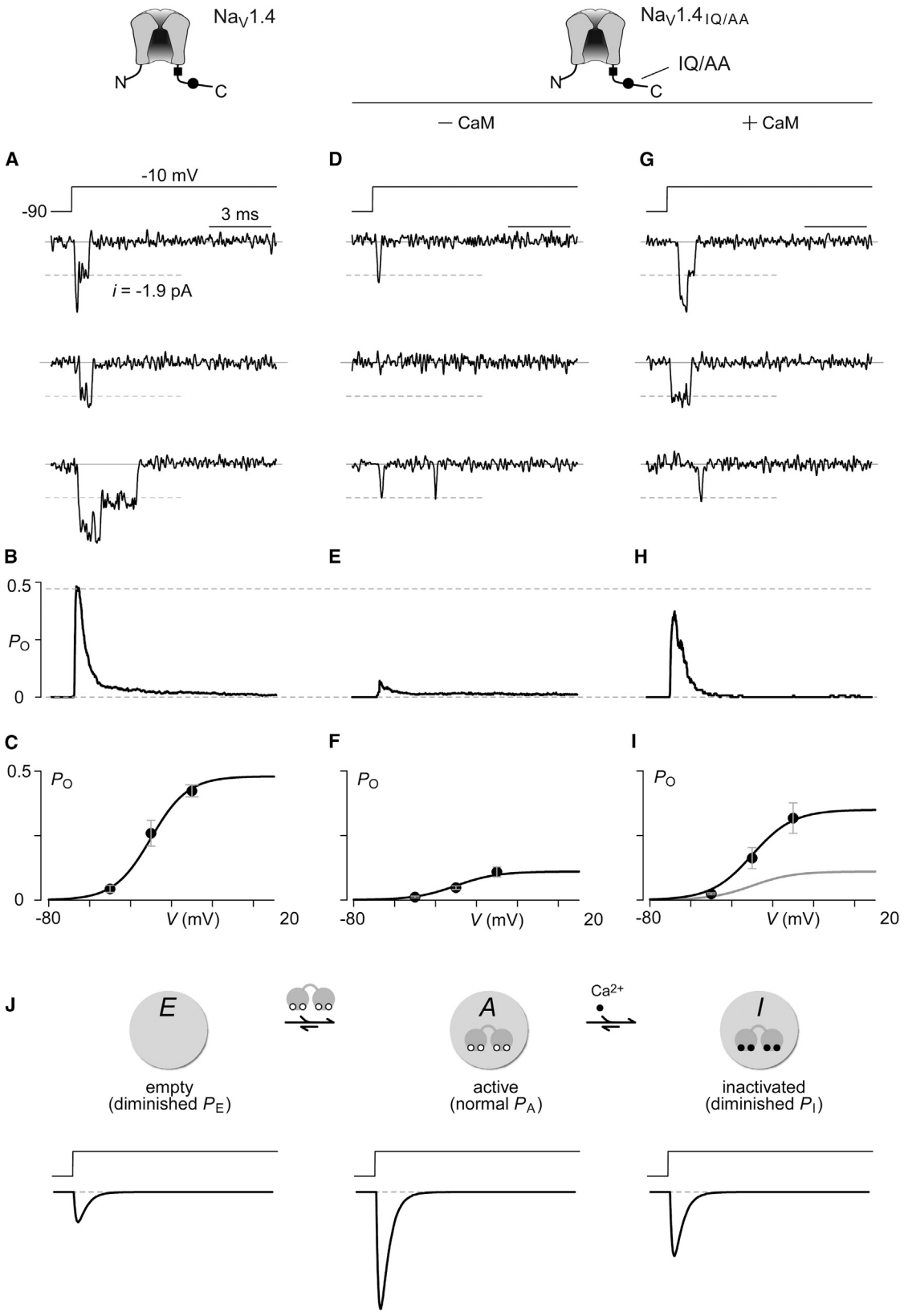

(legend on next page)

$Na_V1.4$ channels have been shown to both reduce CaM binding and decrease current density (Herzog et al., 2003), we undertook direct single-molecule P_O measurements on this particular channel isoform.

To test for apoCaM modulatory effects, we compared the single-channel activity of wild-type $Na_V1.4$ (which avidly binds apoCaM at baseline) with that of a mutant $Na_V1.4_{IQ/AA}$ exhibiting weakened apoCaM affinity via IQ to AA substitution within the IQ domain (Figure S7). Wild-type recombinant $Na_V1.4$ channels exhibited frequent stochastic openings of millisecond duration (Figure 7A). Normalizing the ensemble average of many such records (by unitary current *i* and number of channels *N*) yields a robust P_O waveform that peaks at 0.5 (Figure 7B). This outcome is confirmed by plots of peak P_O versus step potential (Figure 7C), averaged from multiple patches. By contrast, $Na_V1.4_{IQ/AA}$ channels might often lack apoCaM at baseline. Fitting with a mechanism where such channels would be reluctant to open, corresponding single-molecule records display a sparser pattern of activity with briefer openings (Figure 7D). The ensemble average explicitly confirms this impression, yielding a diminutive P_O waveform (Figure 7E) and P_O–*V* relation (Figure 7F). Still, this reduced opening could be an intrinsic effect of mutation, rather than of lacking apoCaM. To exclude the former possibility, we strongly coexpressed CaM with $Na_V1.4_{IQ/AA}$ channels, a maneuver that should restore apoCaM binding via mass action. Reassuringly, corresponding single-molecule records again exhibit robust activity (Figure 7G), and peak P_O is rescued to near wild-type levels (Figures 7H and 7I), confirming a primary action of apoCaM to elevate P_O. These data therefore support conservation of apoCaM modulation of P_O in both Ca_V and Na_V channel superfamilies. As such, like the arrangement for $Ca_V1.3$ channels, we propose that $Na_V1.4$ channels have the potential to reside within one of three configurations (Figure 7J): low P_O configuration *E* lacking apoCaM; high P_O configuration *A* bound to apoCaM; and low P_O configuration *I* bound to Ca^{2+}/CaM. Each configuration may elaborate distinct Na currents upon step depolarization (Figure 7J, bottom subpanels).

DISCUSSION

Apocalmodulin has been traditionally viewed as playing a secondary role to Ca^{2+}/calmodulin for effectuating molecular function (Alberts et al., 1994). More recently, however, there has been growing awareness that apoCaM serves many roles (Jurado et al., 1999). Here, we reveal that apoCaM itself prominently regulates both voltage-gated Ca^{2+} and Na channels. ApoCaM binding to these channels enhances opening several-fold, matching the strongest forms of ion-channel regulation. This effect may unify understanding of a vast array of channel variants and channelopathic mutations that modulate channel affinity for apoCaM. New avenues are thus opened for understanding and manipulating related diseases.

Before turning to broader ramifications, two enabling methodological advances merit attention. First, low-noise single-channel measurements permit direct observation of quantized regulatory phenomena (Figure 2), crucial to deducing mechanism. Second, chemical-dimerizer-based step generation of perimembrane CaM furnishes powerful means to observe CaM-regulatory events in real time within single cells, excluding ambiguities of data drawn from multiple cells and methods. Importantly, a prior strategy for elevating perimembranous CaM requires kinase activation (Yang et al., 2013), potentially complicating discernment of CaM-specific actions. Moreover, our study illustrates the capability of a step generator to resolve biological signal bifurcation upon the binding of a single molecule (apoCaM imparting both an immediate boost in P_O and subsequent CDI); such mechanisms are difficult to prove by customary steady-state methods. Indeed, the overall approach (Figure 3D) mirrors the phase-plane analysis of electronics, highlighting synergy between biological and electrical network analysis (Jack et al., 1975). Biological signal generators and analysis, based not only on perfusable ligands (Spencer et al., 1993) but also on light activation (Hahn and Kuhlman, 2010; Kennedy et al., 2010; Yazawa et al., 2009), may aid future understanding of other signaling systems.

Mechanistic advances for Ca^{2+} channels are 3-fold. First, we discover that apoCaM binding to Ca^{2+} channels strongly elevates P_O by up to 7-fold, before the onset of CDI. At least 2-fold increases of peak current were routinely seen in individual cells undergoing enrichment of apoCaM by rapamycin (Figure 4), but this enhancement is likely a lower bound imposed by limitations of apoCaM recruitment via chemical dimerization (Figure 4B). Using modal analysis of single channels (e.g., Figure 2G), 7-fold augmentation of P_O can be directly deduced. Additionally, the quantitative adherence of all variants to a single line in Figure 5D independently supports this 7-fold P_O modulatory range. That said, the extent of P_O regulation by apoCaM rivals the upregulation of L type Ca^{2+} channels by adrenergic stimulation (Miriyala et al., 2008), the prototypic modulatory system for fight-or-flight responses (Tsien et al., 1986). Second, we unveil an intimate connection between the modulation of P_O and CDI, where the binding of one and the same apoCaM to channels brings not only the ability to undergo CDI as previously reported

Figure 7. ApoCaM Modulates P_O of $Na_V1.4$ Channels

(A) Single-molecule records of wild-type $Na_V1.4$ channels transiently expressed in HEK cells, with only endogenous CaM.

(B) P_O waveform obtained by normalizing ensemble average of >100 records by unitary current *i* and number of channels *N*.

(C) Plot of peak P_O versus step potential (from −90 mV holding potential), averaged over multiple patches. Error bars are ± SEM.

(D) Single-channel records for $Na_V1.4$ channels containing IQ to AA substitution ($Na_V1.4_{IQ/AA}$). Channels are coexpressed with the CaM chelator, $BSCaM_{IQ}$, to minimize free CaM levels (Liu et al., 2010).

(E and F) Corresponding P_O waveform (E) and P_O–*V* relation (F). See also Figure S7.

(G) Single-channel traces for $Na_V1.4_{IQ/AA}$ paired with overexpressed CaM.

(H and I) Corresponding P_O waveform (H) and P_O–*V* relation (I) both restored to near wild-type levels. P_O–*V* relations averaged from n = 5–8 patches each. Error bars, SEM.

(J) Top, proposed Na_V configurations with respect to CaM. Bottom, simulated Na_V currents for configurations above.

(Bazzazi et al., 2013; Ben-Johny et al., 2013; Liu et al., 2010) but also the aforementioned increase of initial P_O. Intriguingly, the P_O of channels lacking CaM (Figure 5E, configuration *E*) seems equivalent to that of channels that have undergone CDI (configuration *I*); in particular, $P_E \sim P_I \sim 0.051$. This outcome is visually confirmed in Figure 4 by the invariance of steady-state current after 300 ms depolarization during rapamycin (see exemplar traces). CDI may thus represent a relinquishing of the initial apoCaM enhancement of P_O. For reference, configurations *A* and *I* in Figure 5E explicitly correspond to proposed molecular arrangements in a prior publication (respectively, Figures 8b and 8c in Ben-Johny et al., 2013). Third, the spectrum of P_O and CDI properties of $Ca_V1.3$ variants (Figure 1A) can now be unified by a single molecular effect—customization of channel binding to apoCaM (Figure 5E). Notably, beyond this specific effect, the properties of variant channels seem largely equivalent once apoCaM becomes bound or unbound. This conclusion is supported by the adherence of all tested variants to a single relation in Figure 5D. One nuance of this unified view may be that the voltage dependence of activation appears subtly different for a variant with an extended DCT that lacks apoCaM (Figures 1E, S1E, and S1F).

The biological implications of these mechanisms are considerable. In particular, the apoCaM affinities of many editing and splice variants are such that natural fluctuations in ambient CaM influence the distribution of channels between pools lacking or armed with apoCaM (Bazzazi et al., 2013; Liu et al., 2010). In switching between pools, we now know that P_O and CDI will be coordinately regulated (Figures 5E and 5F). Furthermore, variants tune not only the midpoint sensitivity to apoCaM at steady state but also the kinetic response to changes in apoCaM (cf., Figures 4D, 4E, and 4F), a property now discernible via CaM step generation. Indeed, it will be important to explore the sequelae of these distinctive kinetic and steady-state properties on Ca^{2+} homeostasis and dysfunction, given CaM variation in physiological and disease conditions (Bezprozvanny, 2009; Black et al., 2004; Bossuyt and Bers, 2013; Chafouleas et al., 1982; Ikeda et al., 2009; Lesnick et al., 2007; Yacoubian et al., 2008). Specifically, given the marked broadening of APs in substantia nigral neurons (Figure 6), it is tempting to speculate that elevated apoCaM predisposes for Ca^{2+}-related neurodegeneration in Parkinson's. Similar modulatory scenarios may pertain throughout the Ca_V1-2 superfamily (Ben-Johny and Yue, 2014), with corresponding biomedical implications. Finally, the mechanisms revealed here (Figures 5E) sharpen distinctions between CaM abnormalities relating to Ca^{2+}/CaM versus apoCaM dysfunction; for example, recently reported CaM missense mutations associated with long-QT syndrome are likely to selectively inhibit transitions into configuration *I* of Ca_V channels (in Figure 5E), while allowing normal access to configuration *A* via maintained binding of Ca^{2+}-free mutant CaMs (Limpitikul et al., 2014).

The extension of like mechanisms to other ion-channel families holds the broadest implications. Only recently have Na channels been shown to exhibit CaM-mediated CDI with similarity to Ca_V channels (Ben-Johny et al., 2014). This likeness is now significantly generalized by our finding that apoCaM also robustly amplifies P_O of $Na_V1.4$ (Figure 7). This conserved modulation in Na channels then suggests that channelopathic disease mutations (Lossin, 2009; Schroeter et al., 2010), RNA editing (Song et al., 2004), and alternative splicing (Lossin, 2009) could all alter apoCaM binding and thereby P_O. The consequences may be extensive, as the $Na_V1.1$-1.9 superfamily governs excitability in brain, heart, and skeletal muscle (Hille, 1984), and related diseases encompass epilepsy, autism, pathological pain, cardiac arrhythmias, and skeletal muscle myotonias (Lossin, 2009; Schroeter et al., 2010). More broadly, numerous other transport molecules bind apoCaM (Bosanac et al., 2005; Saimi and Kung, 2002; Samsó and Wagenknecht, 2002; Vocke et al., 2013; Wen and Levitan, 2002; Xia et al., 1998). Thus, apocalmodulin promises widespread ion-channel regulation whose scope and stature seem likely to proliferate.

EXPERIMENTAL PROCEDURES

Molecular Biology

$Ca_V1.3_S$ and $Ca_V1.3_L$ are identical to previously published rat $Ca_V1.3\Delta$ (AF370009.1) and rat $Ca_V1.3\Delta$ with human long distal carboxyl tail (NM000718), respectively (Liu et al., 2010). $Ca_V1.3_S$ editing/splice variants and apoCaM mutations are the same as those previously published (Bazzazi et al., 2013; Ben-Johny et al., 2013). Lyn-GFP-FRB construct is the same as previously published, and YFP-FKBP-CaM was generated from YFP-FKBP-PI(4)P5K (Ueno et al., 2011). Standard cloning and PCR-based strategies for generating Ca_V variants and FKBP-CaM clones are detailed in Extended Experimental Procedures.

Whole-Cell Electrophysiology

Voltage-clamp and current-clamp whole-cell recording were performed using an Axopatch 200A amplifier. Data were collected and analyzed using custom MATLAB software (Mathworks). Details of recording conditions and recipes for internal and external solutions are specified in Extended Experimental Procedures.

Single-Channel Electrophysiology

Single-channel recordings were performed in the on-cell configuration, using established methods from our laboratory (Tay et al., 2012). To reduce noise, patch pipettes were pulled from ultra-thick-walled borosilicate glass (BF200-116-10, Sutter Instruments) and coated with Sylgard. Recording conditions, data analysis, and recipes for internal and external solutions are provided in Extended Experimental Procedures.

Rapamycin Experiments

Whole-cell currents were recorded for 100 s with regular external solution flowing at 2 ml/min. At 100 s, flow of regular solution was stopped, and flow of the same external containing 200 nM rapamycin was started, triggering dimerization of FRB and FKBP tags that then elevated perimembranous CaM. Flow rates were carefully matched between lines prior to experiments.

Confocal Optical Imaging

Fluorescence images were captured at 20 s intervals, before and after bath application of 200 nM rapamycin. Images were recorded with Olympus Fluoview FV300 and Zeiss LSM710 laser scanning confocal microscopes. Images were analyzed using MATLAB and ImageJ. Details of experimental set-up and data analysis are provided in Extended Experimental Procedures.

SNc Computer Simulation

AP waveforms for substantia nigra dopaminergic neurons were simulated using MATLAB 2010b (Mathworks) based on published models. Details of the model are included in Extended Experimental Procedures and Table S2.

SNc DA Neuron Culture

SNc neurons were isolated from mice expressing GFP under the tyrosine hydroxylase promoter (TH-GFP) (GENSAT; Rockefeller University) (Gong et al.,

2003). Experimental procedures and solution recipes are included in Extended Experimental Procedures.

SUPPLEMENTAL INFORMATION

Supplemental Information includes Extended Experimental Procedures, seven figures, and two tables and can be found with this article online at http://dx.doi.org/10.1016/j.cell.2014.09.047.

AUTHOR CONTRIBUTIONS

P.J.A. performed Ca_V channel experiments and data analysis. M.B.-J. created mutant channels and undertook Na_V experiments and analysis. P.J.A., M.B.-J., and D.T.Y. developed the single-versus-multiple-CaM model. M.B.-J. analyzed fluorescence imaging data and built the SN DA neuron model. I.E.D. supported single-channel data acquisition and analysis and AP analysis. T.I. helped develop the FKBP and FRB CaM system. P.J.A., M.B.-J., and D.T.Y. conceived the project and refined experimental design. P.J.A. and D.T.Y. wrote the paper.

ACKNOWLEDGMENTS

We thank Hojjat Bazzazi and Philemon Yang for providing some $Ca_V1.3$ variants, Ca^{2+} Signals Lab members for valuable comments, and Wanjun Yang for technical support. This work was supported by grants from the NINDS (to D.T.Y.), NHLBI (D.T.Y.), NIMH (M.B.-J.), and Parkinson Society Canada (P.J.A.).

Received: May 19, 2014
Revised: July 25, 2014
Accepted: September 26, 2014
Published: October 23, 2014

REFERENCES

Alberts, B., Bray, D., Lewis, J., Raff, M., Roberts, K., and Watson, J.D. (1994). Molecular Biology of the Cell, Third Edition (New York, London: Garland Publihsing, Inc.).

Bazzazi, H., Ben-Johny, M., Adams, P.J., Soong, T.W., and Yue, D.T. (2013). Continuously tunable $Ca^{(2+)}$ regulation of RNA-edited $Ca_V1.3$ channels. Cell Rep *5*, 367–377.

Bean, B.P. (2007). Neurophysiology: stressful pacemaking. Nature *447*, 1059–1060.

Ben-Johny, M., Yang, P.S., Bazzazi, H., and Yue, D.T. (2013). Dynamic switching of calmodulin interactions underlies Ca2+ regulation of CaV1.3 channels. Nat. Commun. *4*, 1717.

Ben-Johny, M., Yang, P.S., Niu, J., Yang, W., Joshi-Mukherjee, R., and Yue, D.T. (2014). Conservation of Ca^{2+}/calmodulin regulation across Na and Ca^{2+} channels. Cell *157*, 1657–1670.

Ben-Johny, M., and Yue, D.T. (2014). Calmodulin regulation (calmodulation) of voltage-gated calcium channels. J. Gen. Physiol. *143*, 679–692.

Bers, D.M., and Grandi, E. (2009). Calcium/calmodulin-dependent kinase II regulation of cardiac ion channels. J. Cardiovasc. Pharmacol. *54*, 180–187.

Bezprozvanny, I. (2009). Calcium signaling and neurodegenerative diseases. Trends Mol. Med. *15*, 89–100.

Black, D.J., Tran, Q.K., and Persechini, A. (2004). Monitoring the total available calmodulin concentration in intact cells over the physiological range in free Ca^{2+}. Cell Calcium *35*, 415–425.

Bock, G., Gebhart, M., Scharinger, A., Jangsangthong, W., Busquet, P., Poggiani, C., Sartori, S., Mangoni, M.E., Sinnegger-Brauns, M.J., Herzig, S., et al. (2011). Functional properties of a newly identified C-terminal splice variant of $Ca_V1.3$ L-type Ca^{2+} channels. J. Biol. Chem. *286*, 42736–42748.

Bosanac, I., Yamazaki, H., Matsu-Ura, T., Michikawa, T., Mikoshiba, K., and Ikura, M. (2005). Crystal structure of the ligand binding suppressor domain of type 1 inositol 1,4,5-trisphosphate receptor. Mol. Cell *17*, 193–203.

Bossuyt, J., and Bers, D.M. (2013). Visualizing CaMKII and CaM activity: a paradigm of compartmentalized signaling. J. Mol. Med. *91*, 907–916.

Cardozo, D.L., and Bean, B.P. (1995). Voltage-dependent calcium channels in rat midbrain dopamine neurons: modulation by dopamine and GABAB receptors. J. Neurophysiol. *74*, 1137–1148.

Chafouleas, J.G., Bolton, W.E., Hidaka, H., Boyd, A.E., 3rd, and Means, A.R. (1982). Calmodulin and the cell cycle: involvement in regulation of cell-cycle progression. Cell *28*, 41–50.

Chan, C.S., Guzman, J.N., Ilijic, E., Mercer, J.N., Rick, C., Tkatch, T., Meredith, G.E., and Surmeier, D.J. (2007). 'Rejuvenation' protects neurons in mouse models of Parkinson's disease. Nature *447*, 1081–1086.

Chao, S.H., Suzuki, Y., Zysk, J.R., and Cheung, W.Y. (1984). Activation of calmodulin by various metal cations as a function of ionic radius. Mol. Pharmacol. *26*, 75–82.

Christel, C.J., Cardona, N., Mesirca, P., Herrmann, S., Hofmann, F., Striessnig, J., Ludwig, A., Mangoni, M.E., and Lee, A. (2012). Distinct localization and modulation of $Ca_v1.2$ and $Ca_v1.3$ L-type Ca^{2+} channels in mouse sinoatrial node. J. Physiol. *590*, 6327–6342.

Erickson, M.G., Liang, H., Mori, M.X., and Yue, D.T. (2003). FRET two-hybrid mapping reveals function and location of L-type Ca^{2+} channel CaM preassociation. Neuron *39*, 97–107.

Evans, R.M., and Zamponi, G.W. (2006). Presynaptic Ca^{2+} channels—integration centers for neuronal signaling pathways. Trends Neurosci. *29*, 617–624.

Fallon, J.L., Baker, M.R., Xiong, L., Loy, R.E., Yang, G., Dirksen, R.T., Hamilton, S.L., and Quiocho, F.A. (2009). Crystal structure of dimeric cardiac L-type calcium channel regulatory domains bridged by Ca^{2+} calmodulins. Proc. Natl. Acad. Sci. USA *106*, 5135–5140.

Gong, S., Zheng, C., Doughty, M.L., Losos, K., Didkovsky, N., Schambra, U.B., Nowak, N.J., Joyner, A., Leblanc, G., Hatten, M.E., and Heintz, N. (2003). A gene expression atlas of the central nervous system based on bacterial artificial chromosomes. Nature *425*, 917–925.

Grace, A.A., and Bunney, B.S. (1984). The control of firing pattern in nigral dopamine neurons: single spike firing. J. Neurosci. *4*, 2866–2876.

Hahn, K.M., and Kuhlman, B. (2010). Hold me tightly LOV. Nat. Methods *7*, 595–597, 597.

Herzog, R.I., Liu, C., Waxman, S.G., and Cummins, T.R. (2003). Calmodulin binds to the C terminus of sodium channels $Na_v1.4$ and $Na_v1.6$ and differentially modulates their functional properties. J. Neurosci. *23*, 8261–8270.

Hess, P., Lansman, J.B., and Tsien, R.W. (1984). Different modes of Ca channel gating behaviour favoured by dihydropyridine Ca agonists and antagonists. Nature *311*, 538–544.

Hille, B. (1984). Ionic Channels of Excitable Membranes (Sunderland, MA: Sinauer Associates).

Huang, H., Tan, B.Z., Shen, Y., Tao, J., Jiang, F., Sung, Y.Y., Ng, C.K., Raida, M., Köhr, G., Higuchi, M., et al. (2012). RNA editing of the IQ domain in Ca(v)1.3 channels modulates their Ca^{2+}-dependent inactivation. Neuron *73*, 304–316.

Hui, A., Ellinor, P.T., Krizanova, O., Wang, J.J., Diebold, R.J., and Schwartz, A. (1991). Molecular cloning of multiple subtypes of a novel rat brain isoform of the alpha 1 subunit of the voltage-dependent calcium channel. Neuron *7*, 35–44.

Ikeda, S., He, A., Kong, S.W., Lu, J., Bejar, R., Bodyak, N., Lee, K.H., Ma, Q., Kang, P.M., Golub, T.R., and Pu, W.T. (2009). MicroRNA-1 negatively regulates expression of the hypertrophy-associated calmodulin and Mef2a genes. Mol. Cell. Biol. *29*, 2193–2204.

Imredy, J.P., and Yue, D.T. (1994). Mechanism of $Ca^{(2+)}$-sensitive inactivation of L-type Ca^{2+} channels. Neuron *12*, 1301–1318.

Jack, J.J.B., Noble, D., and Tsien, R.W. (1975). Electric Current Flow in Excitable Cells (Oxford, England: Clarendon Press).

Jurado, L.A., Chockalingam, P.S., and Jarrett, H.W. (1999). Apocalmodulin. Physiol. Rev. *79*, 661–682.

Kennedy, M.J., Hughes, R.M., Peteya, L.A., Schwartz, J.W., Ehlers, M.D., and Tucker, C.L. (2010). Rapid blue-light-mediated induction of protein interactions in living cells. Nat. Methods *7*, 973–975.

Kim, E.Y., Rumpf, C.H., Van Petegem, F., Arant, R.J., Findeisen, F., Cooley, E.S., Isacoff, E.Y., and Minor, D.L., Jr. (2010). Multiple C-terminal tail Ca^{2+}/CaMs regulate $Ca_V1.2$ function but do not mediate channel dimerization. EMBO J. *29*, 3924–3938.

Lesnick, T.G., Papapetropoulos, S., Mash, D.C., Ffrench-Mullen, J., Shehadeh, L., de Andrade, M., Henley, J.R., Rocca, W.A., Ahlskog, J.E., and Maraganore, D.M. (2007). A genomic pathway approach to a complex disease: axon guidance and Parkinson disease. PLoS Genet. *3*, e98.

Limpitikul, W.B., Dick, I.E., Joshi-Mukherjee, R., Overgaard, M.T., George, A.L., Jr., and Yue, D.T. (2014). Calmodulin mutations associated with long QT syndrome prevent inactivation of cardiac L-type Ca(2+) currents and promote proarrhythmic behavior in ventricular myocytes. J. Mol. Cell. Cardiol. *74*, 115–124.

Liu, X., Yang, P.S., Yang, W., and Yue, D.T. (2010). Enzyme-inhibitor-like tuning of $Ca^{(2+)}$ channel connectivity with calmodulin. Nature *463*, 968–972.

Lossin, C. (2009). A catalog of SCN1A variants. Brain Dev. *31*, 114–130.

Luik, R.M., Wang, B., Prakriya, M., Wu, M.M., and Lewis, R.S. (2008). Oligomerization of STIM1 couples ER calcium depletion to CRAC channel activation. Nature *454*, 538–542.

Miriyala, J., Nguyen, T., Yue, D.T., and Colecraft, H.M. (2008). Role of Ca_Vbeta subunits, and lack of functional reserve, in protein kinase A modulation of cardiac $Ca_V1.2$ channels. Circ. Res. *102*, e54–e64.

Nedergaard, S. (1999). Regulation of size and excitability in substantia nigra compacta neurons: sensitivity to 4-aminopyridine. J. Neurophysiol. *82*, 2903–2913.

Obeso, J.A., Marin, C., Rodriguez-Oroz, C., Blesa, J., Benitez-Temiño, B., Mena-Segovia, J., Rodríguez, M., and Olanow, C.W. (2008). The basal ganglia in Parkinson's disease: current concepts and unexplained observations. Ann. Neurol. *64* (*Suppl 2*), S30–S46.

Phua, S.C., Pohlmeyer, C., and Inoue, T. (2012). Rapidly relocating molecules between organelles to manipulate small GTPase activity. ACS Chem. Biol. *7*, 1950–1955.

Pitt, G.S., Zühlke, R.D., Hudmon, A., Schulman, H., Reuter, H., and Tsien, R.W. (2001). Molecular basis of calmodulin tethering and Ca^{2+}-dependent inactivation of L-type Ca^{2+} channels. J. Biol. Chem. *276*, 30794–30802.

Puopolo, M., Raviola, E., and Bean, B.P. (2007). Roles of subthreshold calcium current and sodium current in spontaneous firing of mouse midbrain dopamine neurons. J. Neurosci. *27*, 645–656.

Saimi, Y., and Kung, C. (2002). Calmodulin as an ion channel subunit. Annu. Rev. Physiol. *64*, 289–311.

Samsó, M., and Wagenknecht, T. (2002). Apocalmodulin and Ca^{2+}-calmodulin bind to neighboring locations on the ryanodine receptor. J. Biol. Chem. *277*, 1349–1353.

Schroeter, A., Walzik, S., Blechschmidt, S., Haufe, V., Benndorf, K., and Zimmer, T. (2010). Structure and function of splice variants of the cardiac voltage-gated sodium channel $Na_v1.5$. J. Mol. Cell. Cardiol. *49*, 16–24.

Song, W., Liu, Z., Tan, J., Nomura, Y., and Dong, K. (2004). RNA editing generates tissue-specific sodium channels with distinct gating properties. J. Biol. Chem. *279*, 32554–32561.

Spencer, D.M., Wandless, T.J., Schreiber, S.L., and Crabtree, G.R. (1993). Controlling signal transduction with synthetic ligands. Science *262*, 1019–1024.

Suh, B.C., Inoue, T., Meyer, T., and Hille, B. (2006). Rapid chemically induced changes of PtdIns(4,5)P2 gate KCNQ ion channels. Science *314*, 1454–1457.

Tan, B.Z., Jiang, F., Tan, M.Y., Yu, D., Huang, H., Shen, Y., and Soong, T.W. (2011). Functional characterization of alternative splicing in the C terminus of L-type $Ca_V1.3$ channels. J. Biol. Chem. *286*, 42725–42735.

Tay, L.H., Dick, I.E., Yang, W., Mank, M., Griesbeck, O., and Yue, D.T. (2012). Nanodomain Ca^{2+} of Ca^{2+} channels detected by a tethered genetically encoded Ca^{2+} sensor. Nat. Commun. *3*, 778.

Tsien, R.W., Bean, B.P., Hess, P., Lansman, J.B., Nilius, B., and Nowycky, M.C. (1986). Mechanisms of calcium channel modulation by beta-adrenergic agents and dihydropyridine calcium agonists. J. Mol. Cell. Cardiol. *18*, 691–710.

Ueno, T., Falkenburger, B.H., Pohlmeyer, C., and Inoue, T. (2011). Triggering actin comets versus membrane ruffles: distinctive effects of phosphoinositides on actin reorganization. Sci. Signal. *4*, ra87.

Vocke, K., Dauner, K., Hahn, A., Ulbrich, A., Broecker, J., Keller, S., Frings, S., and Möhrlen, F. (2013). Calmodulin-dependent activation and inactivation of anoctamin calcium-gated chloride channels. J. Gen. Physiol. *142*, 381–404.

Wen, H., and Levitan, I.B. (2002). Calmodulin is an auxiliary subunit of KCNQ2/3 potassium channels. J. Neurosci. *22*, 7991–8001.

Xia, X.M., Fakler, B., Rivard, A., Wayman, G., Johnson-Pais, T., Keen, J.E., Ishii, T., Hirschberg, B., Bond, C.T., Lutsenko, S., et al. (1998). Mechanism of calcium gating in small-conductance calcium-activated potassium channels. Nature *395*, 503–507.

Xu, W., and Lipscombe, D. (2001). Neuronal $Ca_V1.3$alpha(1) L-type channels activate at relatively hyperpolarized membrane potentials and are incompletely inhibited by dihydropyridines. J. Neurosci. *21*, 5944–5951.

Yacoubian, T.A., Cantuti-Castelvetri, I., Bouzou, B., Asteris, G., McLean, P.J., Hyman, B.T., and Standaert, D.G. (2008). Transcriptional dysregulation in a transgenic model of Parkinson disease. Neurobiol. Dis. *29*, 515–528.

Yang, T., He, L.L., Chen, M., Fang, K., and Colecraft, H.M. (2013). Bio-inspired voltage-dependent calcium channel blockers. Nat Commun *4*, 2540.

Yazawa, M., Sadaghiani, A.M., Hsueh, B., and Dolmetsch, R.E. (2009). Induction of protein-protein interactions in live cells using light. Nat. Biotechnol. *27*, 941–945.

EXTENDED EXPERIMENTAL PROCEDURES

Molecular Biology

The rat $Ca_V1.3$ "short" ($Ca_V1.3_S$) and $Ca_V1.3$ "long" ($Ca_V1.3_L$) are identical to those previously published as engineered rat $Ca_V1.3\Delta$ (AF370009.1) and rat $Ca_V1.3\Delta$ with human long distal carboxyl tail (NM000718), respectively (Liu et al., 2010). All $Ca_V1.3_S$ variants with either RNA-editing variations ($Ca_V1.3_{S/MQDY}$, $Ca_V1.3_{S/IRDY}$) or apoCaM mutations in the CI region of channels ($Ca_V1.3_{S/TVM\text{-}AAA}$, $Ca_V1.3_{S/LVA\text{-}AAA}$) are the same as previously published (Bazzazi et al., 2013; Ben-Johny et al., 2013). $Ca_V1.3_{S/1.4DCT}$ variant is the $Ca_V1.3_S$ channel backbone fused with the carboxyl tail of $Ca_V1.4$ (Liu et al., 2010). $Na_V1.4$ wild-type and $Na_V1.4$ IQ/AA channels used for single-channel recordings are the same as previously published (Ben-Johny et al., 2014). FRET constructs used were fluorophore-tagged (either enhanced cyan fluorescent protein [ECFP], or yellow fluorescent protein [EYFP]) as previously described (Erickson et al., 2003). The IQ-segment of $Na_V1.4$ wild-type and IQ/AA channels was PCR amplified to include a NotI and XbaI restriction site on the 5′ and 3′ ends respectively, and cloned in frame after the EYFP. The IQ-segment included the amino acid sequence: PITTLKRKQEEVCAIK**IQ(/AA)**RAYRRHLLQRSVKQASYMY. The Lyn-GFP-FRB construct is the same as previously published (Ueno et al., 2011). The YFP-FKBP-CaM construct was generated from a previously published YFP-FKBP-PI(4)P5K construct (Ueno et al., 2011). Wild-type rat CaM was PCR amplified with a 5′ primer incorporating an XhoI site, and a 3′ primer incorporating a BamHI site. The PI(4)P5K insert was removed from the YFP-FKBP construct with 5′ XhoI and 3′ BamHI restriction sites, and replaced in-frame with PCR-amplified wild-type CaM or CaM_{1234} using XhoI and BamHI restriction sites. The linker between FKBP and CaM is 23 amino acids in length and composed of serine-alanine-glycine-glycine repeats. Whereas YFP-FKBP-CaM constructs were used in all electrophysiology recordings, an mCherry-FKBP-CaM construct was used in confocal microscopy experiments to facilitate spectral separation from the Lyn-GFP-FRB construct. All constructs were verified by direct sequencing.

Transfection of HEK293 Cells

For both single-channel and whole-cell electrophysiology, HEK293 cells were transiently transfected using a Ca^{2+} phosphate protocol (Dick et al., 2008). Ten centimeter plates of cells were cotransfected with 8 μg Ca^{2+} channel α_1 subunit for whole-cell electrophysiology experiments, and 2 μg Ca^{2+} channel, or Na channel α_1 subunit for single-channel experiments. Ca^{2+} channel α_1 subunits were coexpressed with 8 μg of rat brain β_{2a} (Perez-Reyes et al., 1992) (M80545) and 8 μg of rat brain $\alpha_2\delta$ (Tomlinson et al., 1993) (NM012919.2). For all whole-cell experiments, 2 μg of SV40 T antigen was cotransfected to enhance expression. When CaM was overexpressed in single-channel experiments, 8–10 μg of cDNA for rat brain wild-type CaM, or CaM_{1234}, was also included in transfections. In Na channel experiment with low CaM, 8 μg of $BSCaM_{IQ}$ was coexpressed (Liu et al., 2010). In whole-cell experiments utilizing rapamycin, 8 μg of cDNA for Lyn-tagged FRB and 2 μg of cDNA for FKBP or FKBP/CaM was used.

Whole-Cell Voltage-Clamp Electrophysiology

Whole-cell recordings were performed at room temperature (20°C–22°C) 24 hr after transfection (Axopatch 200A; Axon Instruments). Patch pipettes (borosilicate glass BF150-86-10; Sutter Instruments) were made using a horizontal puller (P-97; Sutter Instruments Company), fire polished using a microforge (Narishige, Tokyo, Japan), and had typical resistance between 2–3 MΩ when containing internal solution. Upon data collection, P/8 leak subtraction was used, and 70% series resistance and capacitance compensation. Currents were filtered at 2 kHz (four-pole Bessel) and sampled at 10 kHz. Internal solution contained (in mM): 114 cesium methanesulfonate; 5 $CsCl_2$; 1 $MgCl_2$; 4 MgATP; 10 HEPES; 10 BAPTA; at 295 mOsm, adjusted with cesium methanesulfonate; and pH 7.4 adjusted with cesium hydroxide. External solutions contained (in mM): 140 tetraethylammonium methanesulfonate; 10 HEPES; 40 $CaCl_2$; at 300 mOsm, adjusted with tetraethylammonium methanesulfonate; and pH 7.4 adjusted with tetraethylammonium hydroxide. A holding potential of −90 mV, test pulse to +30 mV, and a repetition interval of 20 s were used throughout whole-cell recordings. Data were analyzed using custom MATLAB software (Mathworks); average data are shown as meanc ± SEM.

Whole-Cell Current-Clamp Electrophysiology

Recordings were performed at room temperature (20°C–22°C) (Axopatch 200A; Axon Instruments). Patch pipettes (borosilicate glass BF150-86-10; Sutter Instruments) were made using a horizontal puller (P-97; Sutter Instruments Company), fire polished using a microforge (Narishige, Tokyo, Japan), and had typical resistance between 7–10 MΩ when containing internal solution. Voltage recordings were filtered at 2 kHz (four-pole Bessel) and sampled at 10 kHz. Internal solution contained (in mM): 120 potassium gluconate; 6 NaCl; 4 $MgCl_2$; 5 EGTA; 0.5 $CaCl_2$; 10 Glucose; 10 HEPES; 2 Mg-ATP; 14 Phosphocreatine; at 295 mOsm, adjusted with glucose, and pH 7.4 adjusted with potassium hydroxide. External solution contained (in mM): 137 NaCl; 5.4 KCl; 1.8 $CaCl_2$; 1 $MgCl_2$; 5 HEPES; 10 Glucose; at 300 mOsm, adjusted with Glucose; and pH 7.4 adjusted with NaOH. Recordings were all performed without current injection, to monitor spontaneous activity. Voltage recordings were made for 5 s, with repetition interval of 10 s. Data were analyzed using custom MATLAB software (Mathworks); average data are shown as meanc ± SEM.

Single-Channel Electrophysiology

Cell-attached single-channel recordings were performed at room temperature, using previously established methods from our laboratory (Tay et al., 2012) (Axopatch 200A; Axon Instruments). Patch pipettes (5–10 MΩ) were pulled from ultra-thick-walled borosilicate glass (BF200-116-10, Sutter Instruments), and coated with Sylgard. Currents were filtered at 2–5 kHz. The pipette solution for

Ca^{2+} channel single channel recordings contained (in mM): 140 tetraethylammonium methanesulfonate; 10 HEPES; 40 $BaCl_2$; at 300 mOsm, adjusted with tetraethylammonium methanesulfonate; and pH 7.4 adjusted with tetraethylammonium hydroxide. The pipette solution for Na^+ channel single-channel recordings contained (in mM): 150 NaCl; 10 HEPES; 0.5 $CaCl_2$; at 300 mOsm, adjusted with tetraethylammonium methanesulfonate; and pH 7.4 adjusted with tetraethylammonium hydroxide. To zero membrane potential in all single channel experiments, the bath contained (in mM): 132 K^+-glutamate; 5 KCl; 5 NaCl; 3 MgCl; 2 EGTA; 10 glucose; 20 HEPES; at 300 mOsm adjusted with glucose; and pH 7.4 adjusted with NaOH.

For Ca^{2+} channels, cell-attached single-channel currents were measured during 200 ms voltage ramps between −80 to +70 mV (portions between −50 and 40 mV displayed and analyzed). For each patch, we recorded 100–200 sweeps with a repetition interval of 12 s. Patches with one to three channels were analyzed as follows: (1) The leak for each sweep was fit and subtracted from each trace. (2) The unitary current relation, $i(V)$, was fit to the open-channel current level using the following equation (Hille, 1984) (Figures 1D–1K, slanted gray line):

$$i(V) = -g \cdot (V - V_S) \cdot \exp(-(V - V_S) \cdot z \cdot F/(R \cdot T))/(1 - \exp(-(V - V_S) \cdot z \cdot F/(R \cdot T)))$$

where g is the single-channel conductance (~0.2 pA/mV), z is the apparent valence of permeation (~2.1), F is Faraday's constant, R is the gas constant, and T is the temperature in degrees Kelvin (assumed room temperature). All these parameters were held constant for all patches, except for slight variations in the voltage-shift parameter V_s ~35 mV, as detailed below. (3) All leak-subtracted traces for each patch were averaged (and divided by the number of channels in the patch) to yield an I–V relation for that patch. Since slight variability in V_S was observed among patches, we calculated an average V_S for each construct, $V_{S,AVE}$. The data from each patch were then shifted slightly in voltage by an amount $\Delta V = V_{S,AVE} - V_S$, with ΔV typically about ± 5 mV. This maneuver allowed all patches for a given construct to share a common open-channel GHK relation. Thus shifted, the I–V relations obtained from different patches for each construct were then averaged together. (4) P_O at each voltage was determined by dividing the average I (determined in step 3 above) into the open-channel GHK relation. Channel number was determined by the maximal number of overlapping opening events upon application of the channel agonist Bay K8644 (5 μM) at the end of each recording.

For Na^+ channels, cell-attached single-channel currents were measured during 50 ms voltage steps to −50 mV, −30 mV, and −10 mV, from a holding of −90 mV. For each patch, we recorded 100–800 sweeps with a repetition interval of 5 s. The leak for each sweep was fit and subtracted. All leak subtracted sweeps in each patch were averaged to obtain average current (I). P_O at each voltage was determined by dividing the average I by the unitary current ($N\,i$). Channel number N was determined by open channel stacking and noise analysis (Sigworth, 1981).

For statistical analysis of quantized modal gating, we explicitly performed Hartigan's dip test on sweep histograms of $\overline{P}_O$ (Amini et al., 1999; Hartigan and Hartigan, 1985). The dip test was performed on $\ln \overline{P}_O$, utilizing 500 bootstrap steps. This analysis supports the use of bimodal fits when employed (Figures 2E–2H, S1, S2A–S2D, and S2G–S2L), and unimodal fits in other cases (Figures 2A–2D, S2E, and S2F). Outcomes of the dip analysis are stated in the appropriate figure legends.

Rapamycin Experiments

Whole-cell voltage-clamp experiments were performed as described above. 300 ms voltage steps to +30 mV from −90 mV holding were performed every 20 s for an initial 100 s with regular external solution (above) flowing at 2 ml/min. At 100 s, flow of regular external solution was stopped, and flow of the same external containing 200 nM rapamycin was started. Flow rates where carefully matched between lines prior to experiments.

Confocal Optical Imaging

HEK293 cells were transiently transfected with the same FRB and FKBP constructs, under identical conditions as described for whole-cell electrophysiology above. Fluorescence images were obtained every 20 s, before and after bath application of 200 nM rapamycin. Fluorescence measurements were performed with either an Olympus Fluoview FV300 confocal laser scanning microscope, or an LSM710 confocal microscope (Carl Zeiss). For the FV300 unit, we used an Olympus PlanApo 40× or 60× oil objective (NA 1.40, PLAPO60XO3; Olympus). Excitation light was generated with either an Argon Laser (488 nm) for GFP excitation, or a Helium Neon (HeNe) Green Laser for mCherry excitation. The following Olympus optical filters were used: 442/515 nm excitation splitter (FV-FCV) and 515 nm emission splitter (FV-515CH). GFP emission channel contained BA510 IF and BA530RIF filters. The mCherry channel contained a 605BP filter. Fluorescent images were collected using the Fluoview software (Olympus). Closely similar optical parameters and elements were used with the LSM710 platform. Images were analyzed using MATLAB and ImageJ. For each cell, fluorescence intensity measured along many line segments was fit with two Gaussian functions approximating membrane fluorescence. Membrane boundaries were defined by peak GFP signal from Lyn-GFP-FRB.

Quantitative Simulation of SNc Dopaminergic Neuron Activity

Action potential waveforms for substantia nigra dopaminergic neurons in Figure 6 were simulated using MATLAB 2010b (Mathworks) based on published models (Amini et al., 1999; Chan et al., 2007). The model assumes a spherical geometry for the soma with diameter of 20 μm. Calcium diffusion within the soma is modeled as described previously with four radial shell compartments (Tay et al., 2012). Ca^{2+} influx through L type Ca^{2+} channel on the superficial surface injects Ca^{2+} into the outermost shell, and whole-cell pipette

allows the gradual egress of Ca^{2+} from the cell center (Tay et al., 2012). The time-dependent changes in membrane potential is computed by solving the ordinary differential equation,

$$\frac{dV}{dt} = -\frac{1}{C_m}(I_{Na} + I_{Ca\text{-}L} + I_K + I_A + I_{SK} + I_{leak})$$

where C_m is the normalized membrane capacitance assumed to be 1 $\mu F/cm^2$. Model currents included sodium current (I_{Na}), calcium current through $Ca_V1.3$ channels ($I_{Ca\text{-}L}$), delayed rectifier potassium current (I_K), transient outward potassium current (I_A), Ca^{2+} activated potassium current (I_{SK}) and a leak current (I_{leak}). The biophysical model for these currents and relevant parameters along with relevant references are tabulated in Table S2.

SNc DA Neuron Culture

SNc neurons were isolated from mice expressing GFP under the tyrosine hydroxylase promoter (TH-GFP) (GENSAT; Rockefeller University) (Gong et al., 2003). Brains from TH-GFP mice were rapidly removed after decapitation and placed in ice-cold solution containing the following (in mM): 59.4 NaCl; 25 $NaHCO_3$; 25 glucose; 75 sucrose; 2.5 KCl; 2.3 NaH_2PO_4; 0.9 $CaCl_2$; 14.9 $MgCl_2$. Brains were sectioned into 400 μm coronal slices, and SNc dissected using a 22 gauge needle. SNc were enzymatically digested with 3 mg/ml of proteinase XXIII (Sigma) for 1 hr at 37°C in dissociation solution containing (in mM): 82 $NaSO_4$; 30 K_2SO_4; 10 HEPES; 10 glucose; 5 $MgCl_2$; at 305–310 mOsm adjusted with glucose and pH 7.4 adjusted with NaOH. All solutions were continuously bubbled with 95% O_2, 5% CO_2. Following digestion, pieces were washed in Tyrode's solution containing (in mM): 150 NaCl; 4 KCl; 2 $CaCl_2$; 10 glucose; and 10 HEPES; at 305–310 mOsm adjusted with glucose and pH 7.4 adjusted with NaOH. Tyrode's solution was supplemented with 1 mg/ml of bovine serum albumin and trypsin inhibitor. After wash, SNc were moved to DMEM/F12 GlutaMAX (GIBCO) supplemented with 3% FBS, N2 supplement, B27 supplement, NEAA, and glia-derived neurotrophic factor (GDNF) (25 ng/ml). Pieces were triturated with a series of glass pipettes and plated on glass coverslips coated with poly-L-lysine, and incubated at 37°C, and 5% CO_2 until experiments performed between 1 and 7 days later.

SUPPLEMENTAL REFERENCES

Amini, B., Clark, J.W., Jr., and Canavier, C.C. (1999). Calcium dynamics underlying pacemaker-like and burst firing oscillations in midbrain dopaminergic neurons: a computational study. J. Neurophysiol. *82*, 2249–2261.

Dick, I.E., Tadross, M.R., Liang, H., Tay, L.H., Yang, W., and Yue, D.T. (2008). A modular switch for spatial Ca^{2+} selectivity in the calmodulin regulation of Ca_V channels. Nature *451*, 830–834.

Hartigan, J.A., and Hartigan, P.M. (1985). The dip test of unimodality. Ann. Stat. *13*, 70–84.

Hirschberg, B., Maylie, J., Adelman, J.P., and Marrion, N.V. (1998). Gating of recombinant small-conductance Ca-activated K^+ channels by calcium. J. Gen. Physiol. *111*, 565–581.

Johnson, K.J. (1980). Numerical Methods in Chemistry (New York: Marcel Dekker).

Luo, C.H., and Rudy, Y. (1991). A model of the ventricular cardiac. Depolarization, repolarization, and their interaction. Circ. Res. *68*, 1501–1526.

Mori, M.X., Erickson, M.G., and Yue, D.T. (2004). Functional stoichiometry and local enrichment of calmodulin interacting with Ca^{2+} channels. Science *304*, 432–435.

Perez-Reyes, E., Castellano, A., Kim, H.S., Bertrand, P., Baggstrom, E., Lacerda, A.E., Wei, X.Y., and Birnbaumer, L. (1992). Cloning and expression of a cardiac/brain beta subunit of the L-type calcium channel. J. Biol. Chem. *267*, 1792–1797.

Sang, L., Bazzazi, H., Ben-Johny, M., and Yue, D.T. (2012). Resolving the grip of the distal carboxy tail on the proximal calmodulatory region of Ca_V channels (abstr.). Biophys. J. *102*, 126a.

Sigworth, F.J. (1981). Covariance of nonstationary sodium current fluctuations at the node of Ranvier. Biophys. J. *34*, 111–133.

Singh, A., Gebhart, M., Fritsch, R., Sinnegger-Brauns, M.J., Poggiani, C., Hoda, J.C., Engel, J., Romanin, C., Striessnig, J., and Koschak, A. (2008). Modulation of voltage- and Ca^{2+}-dependent gating of $Ca_V1.3$ L-type calcium channels by alternative splicing of a C-terminal regulatory domain. J. Biol. Chem. *283*, 20733–20744.

Tomlinson, W.J., Stea, A., Bourinet, E., Charnet, P., Nargeot, J., and Snutch, T.P. (1993). Functional properties of a neuronal class C L-type calcium channel. Neuropharmacology *32*, 1117–1126.

Yang, P.S., Ben-Johny, M., and Yue, D.T. (2014). Allostery in Ca^{2+} channel modulation by calcium-binding proteins. Nat. Chem. Biol. *10*, 231–238.

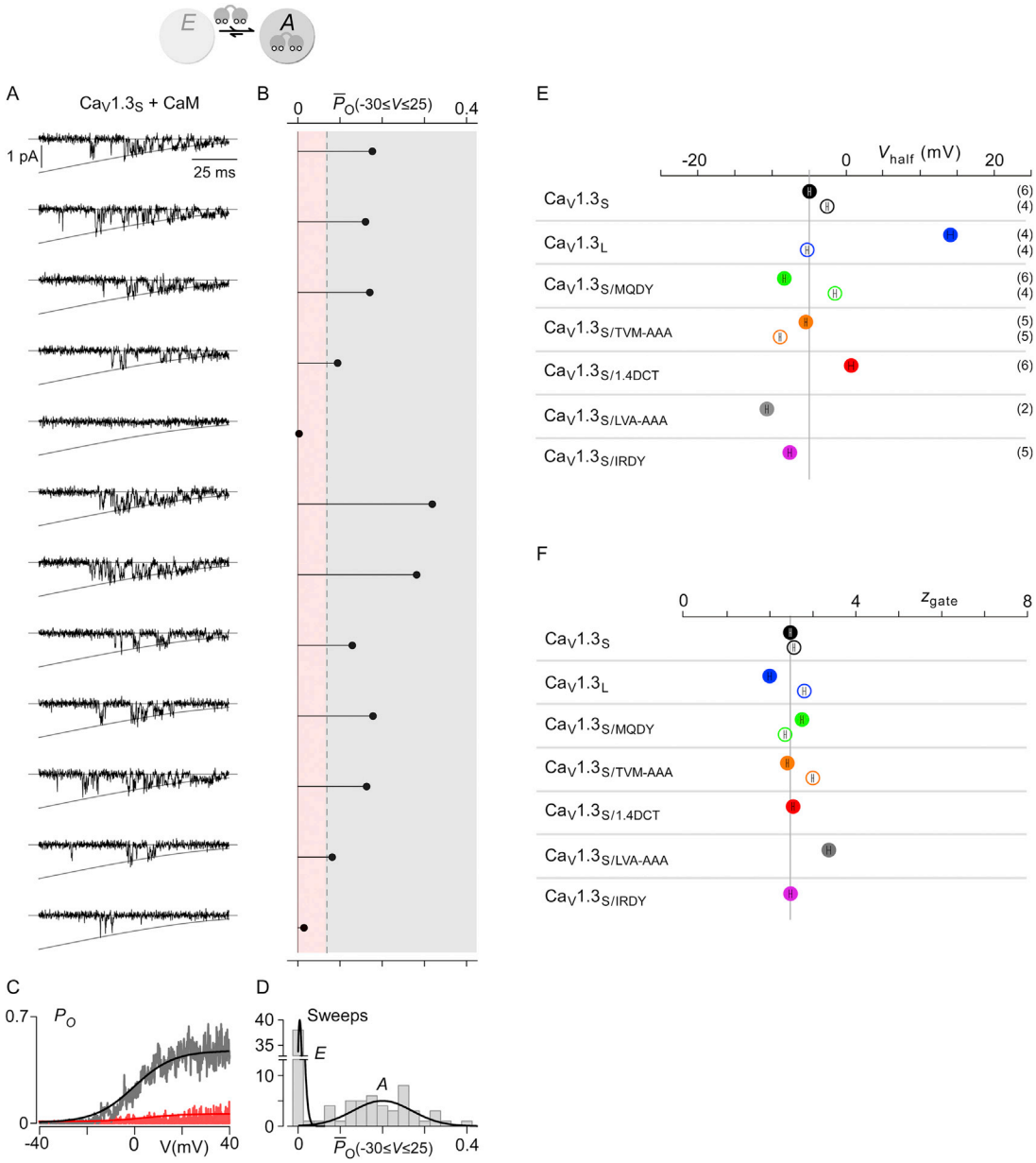

Figure S1. Quantized Modal Analysis for $Ca_V1.3_S$, Related to Figure 2

(A) $Ca_V1.3_S$ channels expressed in HEK cells with CaM overexpression are expected to predominantly occupy configuration *A* (top cartoon). Representative single-channel Ba^{2+} currents elicited during voltage ramp shown between −40 and +40 mV reveals that channel resides mostly within a high P_O gating mode.

(B) For each trace in (A), an average P_O was calculated for voltages between −30 and +25 mV ($\overline{P}_O$ [$-30 \leq V \leq 25$]). Red shaded region corresponds to low P_O range, and gray shaded region corresponds to high P_O range.

(C) Average P_O at each voltage between −40 and +40 mV was calculated for low P_O sweeps (red trace) and high P_O sweeps (gray traces).

(D) Number of sweeps with $\overline{P}_O$ ($-30 \leq V \leq 25$) within indicated P_O ranges. Data shows two predominant P_O modes, low P_O mode encompassing channels in configuration *E*, and high P_O mode encompassing channels in configuration *A*. $\overline{P}_O$ histogram was inconsistent with unimodal distribution ($p < 0.001$, Hartigan's dip test) and therefore fit with bimodal distribution functions.

(E) Population data summarizing voltage dependence of single-channel activation (V_{half} is the voltage yielding half maximal P_O) for the various recombinant $Ca_V1.3$ isoforms. Filled circles are for data obtained with only endogenous CaM present, and open circles during CaM overexpression. In parentheses on right, number of patches from which P_O–*V* relations were averaged and analyzed. Jacobian error matrix analysis (Johnson, 1980) was used to estimate standard deviations (±error bars in this panel). Only the $Ca_V1.3_L$ channel (with only endogenous CaM present) shows an appreciable right shift in the voltage dependence of activation (Singh et al., 2008), and CaM overexpression returns V_{half} to values observed with $Ca_V1.3_S$ channels.

(F) Population data summarizing the slope (z_{gate}) for a Boltzmann relation fit to P_O–*V* relations for the indicated $Ca_V1.3$ isoforms. Filled circles are data obtained with only endogenous CaM present, and open circles data during CaM overexpression.

Numbers in parentheses on right of (E) are relevant to this panel as well. Error bars are ± SD, determined by Jacobian error matrix analysis as in (E).

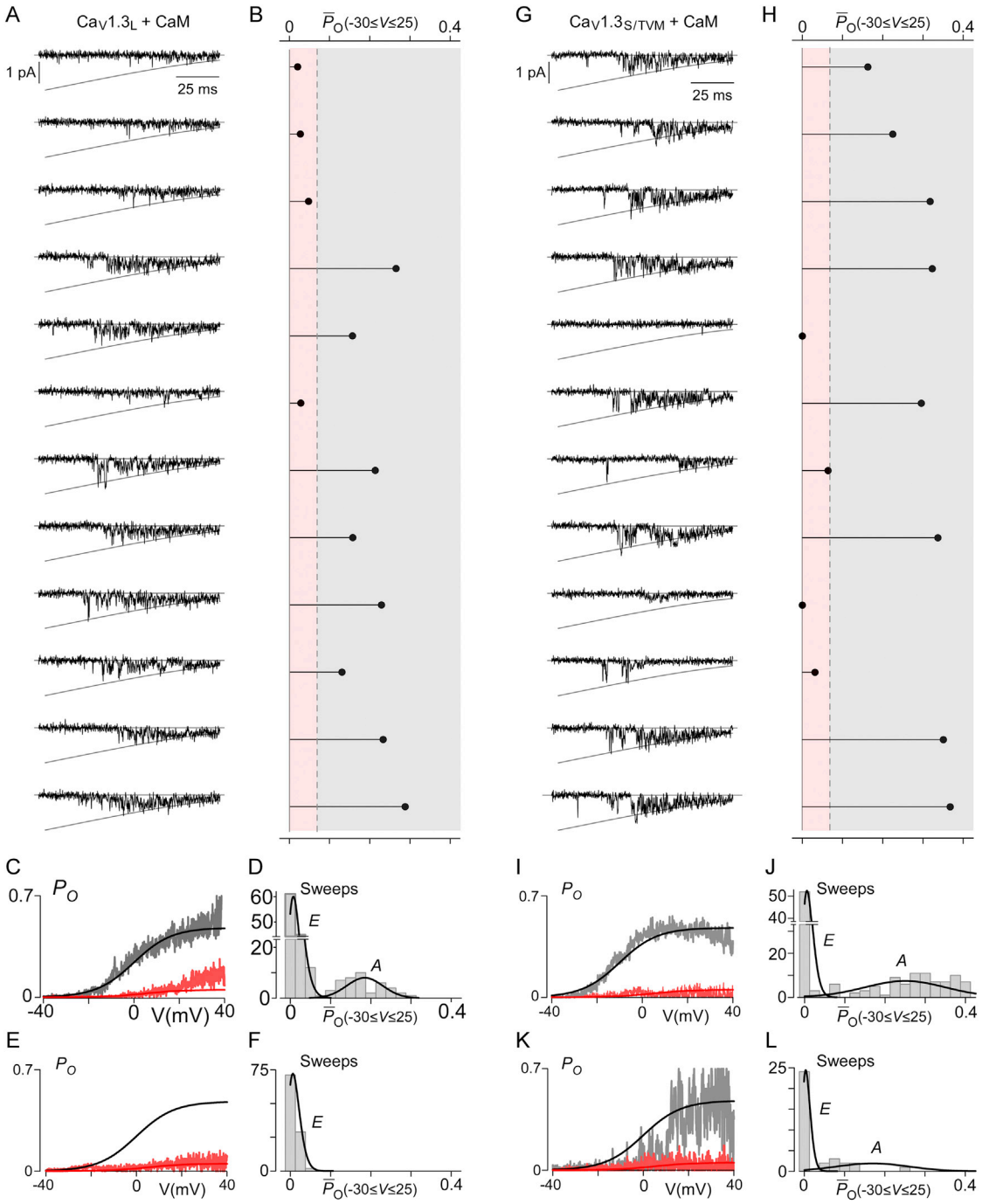

Figure S2. Quantized Modal Analysis for $Ca_V1.3_L$ and $Ca_V1.3_{S/TVM\text{-}AAA}$, Related to Figure 2

(A) $Ca_V1.3_L$ channels expressed in HEK cells with CaM overexpression are expected to largely occupy configuration *A*. Representative single-channel Ba^{2+} currents elicited during voltage ramp between −40 and +40 mV illustrates mostly high P_O gating activity.

(B) For each trace in (A), an average P_O was calculated for voltages between −30 and +25 mV ($\overline{P}_O$ [$-30 \leq V \leq 25$]). Red shaded region corresponds to low P_O range, and gray shaded region corresponds to high P_O range.

(C) Average P_O at each voltage between −40 and +40 mV was calculated for low P_O sweeps (red trace) and high P_O sweeps (gray traces). Fits reproduced from Figure S1 for comparison.

(D) Number of sweeps with $\overline{P}_O$ ($-30 \leq V \leq 25$) within indicated P_O ranges. Data show two predominant P_O modes, low P_O mode encompassing channels in configuration *E*, and high P_O mode incorporating channels in configuration *A*. $\overline{P}_O$ histogram was inconsistent with unimodal distribution ($p < 0.001$, Hartigan's dip test) and therefore fit with bimodal distribution functions.

(legend continued on next page)

(E and F) Conversely, $Ca_V1.3_L$ channels expressed in HEK cells with endogenous levels of CaM reside predominantly within configuration *E* and have single-channel records showing a single low P_O gating mode. Histogram was consistent with unimodal distribution ($p > 0.08$) by Hartigan's dip test. Fits reproduced from Figure S1 for comparison.
(G–L) Same single-channel analysis for the $Ca_V1.3_{S/TVM\text{-}AAA}$ channel.

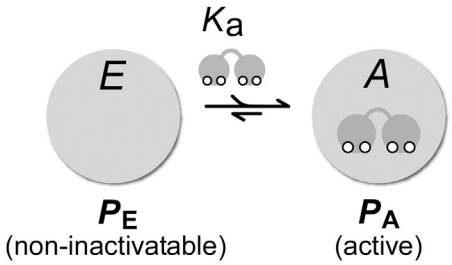

Figure S3. Channel Baseline P_O as a Consequence of Direct ApoCaM Binding, Related to Figure 3

We here consider aggregate baseline P_O ($P_{CaM/endo}$) measured with only endogenous CaM present, and using Ba^{2+} as the charge carrier to preclude CDI. To deduce an explicit Langmuir relation between $P_{CaM/endo}$ and the association constant for apoCaM binding to channels (K_a), we consider the transition from a channel configuration lacking an apoCaM (configuration *E*) to a configuration charged with an onboard apoCaM (configuration *A*). P_E and P_A, respectively, represent the open probabilities for channels in configurations *E* ("empty," or noninactivatable) and *A* ("active"). If $f_{b/CaM/endo}$ represents the steady-state fraction of channels bound to an onboard apoCaM at endogenous concentrations of apoCaM, then

$$P_{CaM/endo} = P_E \cdot \left(1 - f_{b/CaM/endo}\right) + P_A \cdot f_{b/CaM/endo} \quad \text{(S1)}$$

Rearranging this equation,

$$P_{CaM/endo} = P_E + \left(P_A - P_E\right) \cdot f_{b/CaM/endo} \quad \text{(S2)}$$

The steady-state fraction of channels bound to an apoCaM under these conditions is given by the following (Ben-Johny et al., 2013):

$$f_{b/CaM/endo} = K_a \cdot \left(K_a + \Lambda\right)^{-1}$$

where $\Lambda \propto [\text{apoCaM}_{bulk}]^{-1}$, and where apoCaM_{bulk} is the free concentration of apoCaM in the bulk cytoplasm. Substituting this relationship into Equation S2, we obtain:

$$P_{CaM/endo} = P_E + \left(P_A - P_E\right) \cdot K_a \cdot \left(K_a + \Lambda\right)^{-1} \quad \text{(S3)}$$

Here, the apoCaM binding affinity (K_a) for the different channel variants and mutants are estimated by previously published, live-cell FRET 2-hybrid assays (Bazzazi et al., 2013; Ben-Johny et al., 2013) (Table S1). Thus, if apoCaM modulates channel P_O, $P_{CaM\text{-}endo}$ should relate to apoCaM binding (K_a) by the Langmuir relationship in Equation S3. P_E is the open probability of channels residing in configuration *E*, measured to be 0.051 in main text Figure 3C. P_A is the open probability of channels residing in configuration A, measured to be 0.33 in main text Figure 1H. This value is confirmed from the modal analysis of high P_O sweeps in Figure S1C (gray trace fit, yielding plateau P_O = 0.45), after taking into account an ~30% fraction of blank sweeps (0.45 × 0.7 = 0.32).

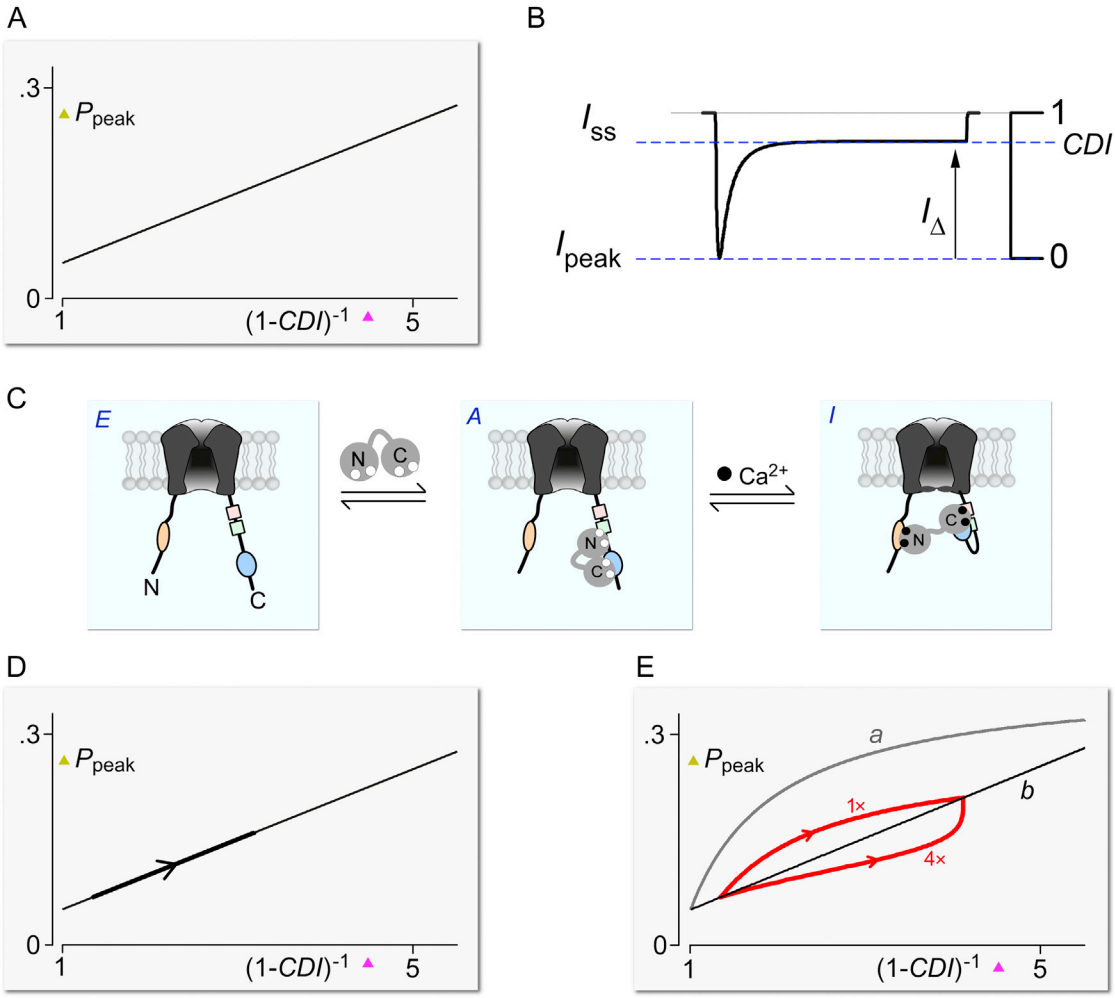

Figure S4. Derivation of Main-Text Equation 2, Related to Figure 3

(A) Linear P_O versus *CDI* relation reproduced from main-text Figure 3D (thin black line), as given by main-text Equation 2, reproduced here for convenience.

$$I_{peak}/I_{max} = P_E \cdot (1 - CDI)^{-1} \quad \text{(S4)}$$

I_{peak} is the peak Ca^{2+} current before and during rapamycin application in main text Figure 4. I_{max} would be the peak current if all channels in a cell were simultaneously open. P_E is the open probability of channels residing in configuration *E* (see panel C), measured to be 0.051 in main text Figure 3C. *CDI* is our standard metric of CDI strength, defined as I_Δ / I_{peak} in panel B. $P_{peak} = I_{peak} / (N\,i)$, where *N* is the number of channels within a particular cell, and *i* is the unitary current during activating voltage steps (measured directly from single-channel experiments).

(B) Definition of I_{peak} and *CDI* as defined for schematized whole-cell Ca^{2+} current.

(C) Configuration *E* (left subpanel) cartoons channels lacking apoCaM. P_E is the open probability of channels in this configuration. Configuration *A* (middle subpanel) portrays a channel with apoCaM bound, poised at the ready to undergo CDI. Channels in configuration *A* would gate with an open probability of P_A. Ca^{2+} binding to the resident CaM drives channels into configuration *I* (Ca^{2+} inactivated, right subpanel), where channels gate with open probability P_I. The P_O values used to analyze whole-cell currents evoked by steps to + 30 mV (analysis in Figure 5) were taken from the plateau values of experimental single-channel P_O–*V* relations. In particular, if we account for a small 8 mV surface-charge shift between the 40 mM Ba^{2+} conditions used for single-channel recordings, and the 40-mM Ca^{2+} configuration used for whole-cell recordings in rapamycin experiments, the whole-cell currents would reference single-channel P_O values at +22 mV, on the plateau of single-channel P_O–*V* relations. Equation S4 was thus derived as follows. *I*peak would be given by

$$I_{peak} = f_b \cdot P_A \cdot N \cdot i + (1 - f_b) \cdot P_E \cdot N \cdot i \quad \text{(S5)}$$

where f_b is the fraction of channels bound to apoCaM (whether or not the system is at steady state). Our standard *CDI* metric can be explicitly related to measurable attributes of currents (defined in panel B) according to the relation

$$CDI = (I_{peak} - I_{SS})/I_{peak} \quad \text{(S6)}$$

Rearranging gives,

(legend continued on next page)

$$I_{peak} = (1 - CDI)^{-1} \cdot I_{SS} \tag{S7}$$

and I_{SS} can be expressed as the weighted sum of various open probabilities as

$$I_{SS} = [f_b((1 - F_{CDI}) \cdot P_A + F_{CDI} \cdot P_I)]Ni + [(1 - f_b) \cdot P_E]Ni \tag{S8}$$

where F_{CDI} refers to the fraction of channels charged with apoCaM that actually undergo CDI at steady state. In main-text Figures 4D–4F (exemplar traces), a striking empirical result is that I_{SS} remains constant upon application of rapamycin (which changes f_b). This result implies that

$$0 = \frac{dI_{SS}}{df_b} \Rightarrow P_E = (1 - F_{CDI}) \cdot P_A \cdot F_{CDI} \cdot P_I \tag{S9}$$

Substituting Equation S9 into S8 then yields:

$$I_{SS} = P_E \cdot N \cdot i \tag{S10}$$

Substituting Equation S10 into Equation S7 yields

$$I_{peak} = (1 - CDI)^{-1} \cdot P_E \cdot N \cdot i \tag{S11}$$

and dividing both sides by I_{max} (= N i) gives Equation S4, which is main-text Equation 2. One additional note warrants mentions. Equation S9 furnishes an intriguing constraint on the value of P_I. Since F_{CDI} must be bounded between 0 and 1, Equation S9 then constrains P_I to the range $0 \leq P_I \leq P_E$ (where P_E is measured to be 0.051 in main text Figure 3C). Moreover, to satisfy Equation S9 from a purely mathematical perspective, each specific value of P_I within this range must be paired with a particular value of F_{CDI}. The most plausible physical realization of this mathematical constraint is for the Ca^{2+} influx through channels and affinities of channel effector sites for Ca^{2+}/CaM to suffice to fully engage CDI (F_{CDI} driven toward 1), and for $P_I = P_E$. The latter statement would imply that CDI is equivalent simply to the relinquishing of the initial effect of apoCaM binding to boost P_O (from P_E to P_A).

(D) Simulated P_{peak} and *CDI* relationship for single CaM model during rapid CaM step. Initial conditions were calculated for a starting apoCaM concentration of 0.1 μM and K_d for apoCaM association of 1.5 μM. These yield the P_{peak} versus $(1-CDI)^{-1}$ data point residing on the left edge of the thick line segment, overlying the thin black line corresponding to Equation S4. A step increase in apoCaM concentration (0.1 to 2 μM) was then applied, and numerical simulations were used to predict the extent of apoCaM binding as a function of time. If a single CaM drives both P_{peak} and *CDI,* even though apoCaM binding to channels would deviate from equilibrium during such a transition, all P_{peak} versus $(1-CDI)^{-1}$ points would nonetheless reside on the same line (thick black arrow trajectory). This feature arises because each point on the trajectory corresponds to a specific fraction of channels bound to apoCaM, and each fraction enforces a unique pairing of P_{peak} versus $(1-CDI)^{-1}$ values.

(E) Simulated P_{peak} versus $(1-CDI)^{-1}$ relation for two-CaM model during rapid CaM step. We consider a system where apoCaM binding to one site enables CDI to occur, and apoCaM binding to an alternate site increases baseline P_O (prior to CDI), from P_E to P_A. ApoCaM binding to these sites is assumed to occur independently, and the steady-state fraction of peak current remaining after CDI is set to reproduce the experimentally observed CDI in $Ca_V1.3_S$ (Ben-Johny et al., 2013). Thin gray line (*a*) plots the steady-state relationship between P_{peak} versus $(1-CDI)^{-1}$ if the dissociation constants for apoCaM binding to P_O ($K_{d|P}$) and CDI ($K_{d|CDI}$) sites were equivalent at 1.5 μM. The thin black line (*b*) plots the steady-state P_{peak} versus $(1-CDI)^{-1}$ relation if $K_{d|CDI}$ were to equal $K_{d|P} \cdot P_E/P_A$. However, in this case, the difference in dissociation constants at the two sites means that the transient response to abrupt changes in apoCaM would deviate from the linear steady-state relation if the *CDI* regulatory site loads at the same rate (1×) or 4-fold faster (4×) than the P_O site, as shown by the red trajectories. Simulations were performed in MATLAB using the matrix exponential function.

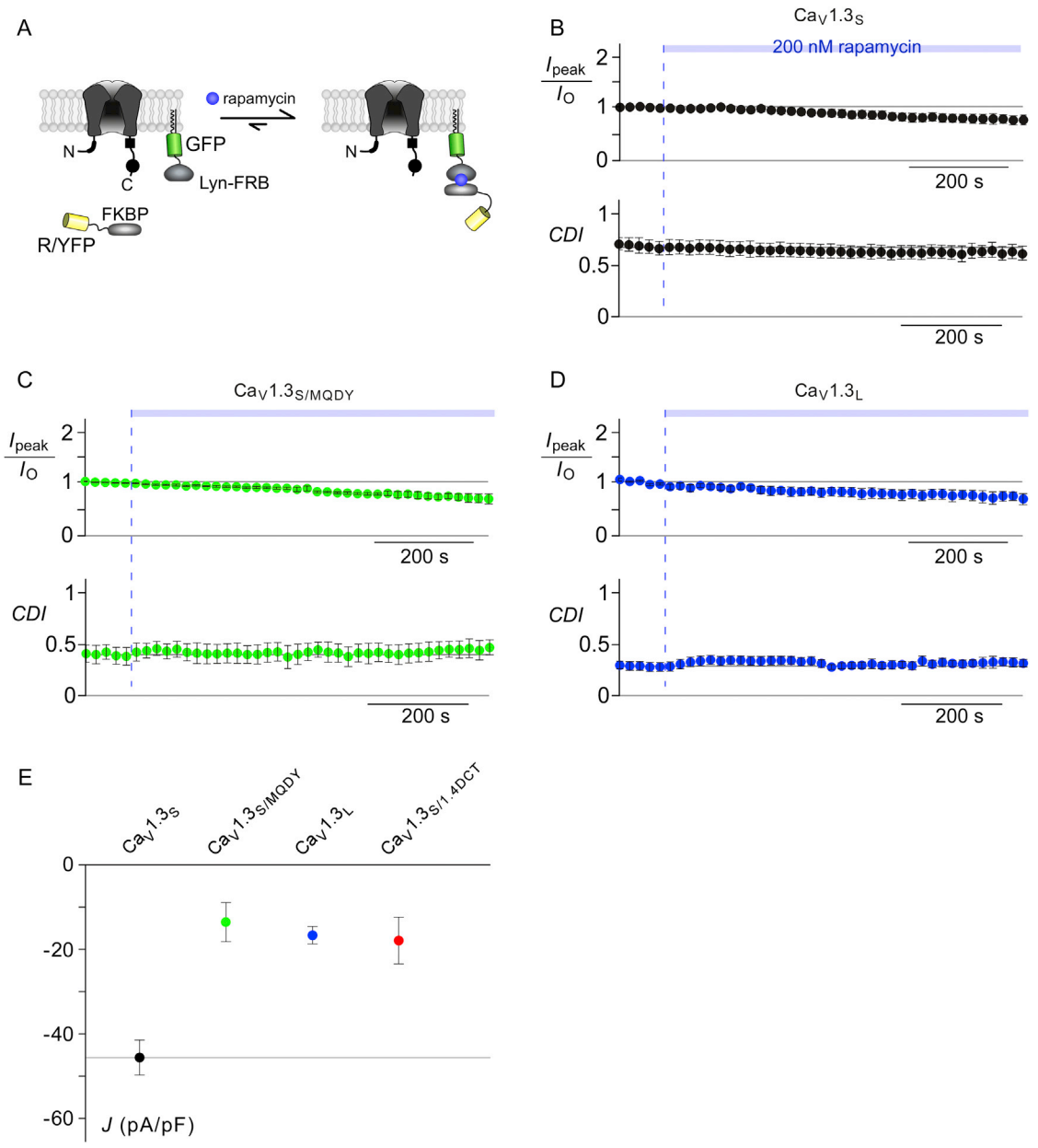

Figure S5. FRB-FKBP Control, Related to Figure 4

(A) FKBP without CaM was recruited to the membrane by rapamycin in HEK293 cells transiently expressing $Ca_V1.3$ channels.

(B) $Ca_V1.3$ short variant channels ($Ca_V1.3_S$; black symbols) showed no change in either normalized peak current (top) or *CDI* (bottom), upon FKBP recruitment to the membrane.

(C and D) RNA-edited $Ca_V1.3$ channels ($Ca_V1.3_{S/MQDY}$, green symbols) and $Ca_V1.3$ long-variant channels ($Ca_V1.3_L$, blue symbols) were also unaffected by FKBP localization to the membrane. All averages derived from multiple cells (n = 3–9). Error bars are ± SEM throughout. These data confirm that CaM (and not FKBP) is indeed responsible for the enhanced peak current (P_O) and CDI seen in the main text.

(E) Current density (*J*) measured at +30 mV for all indicated $Ca_V1.3$ isoforms with only endogenous CaM present. On average, channel variants lacking apoCaM exhibited lower current densities than $Ca_V1.3_S$, consistent with predicted lower open probabilities (main text Figure 1).

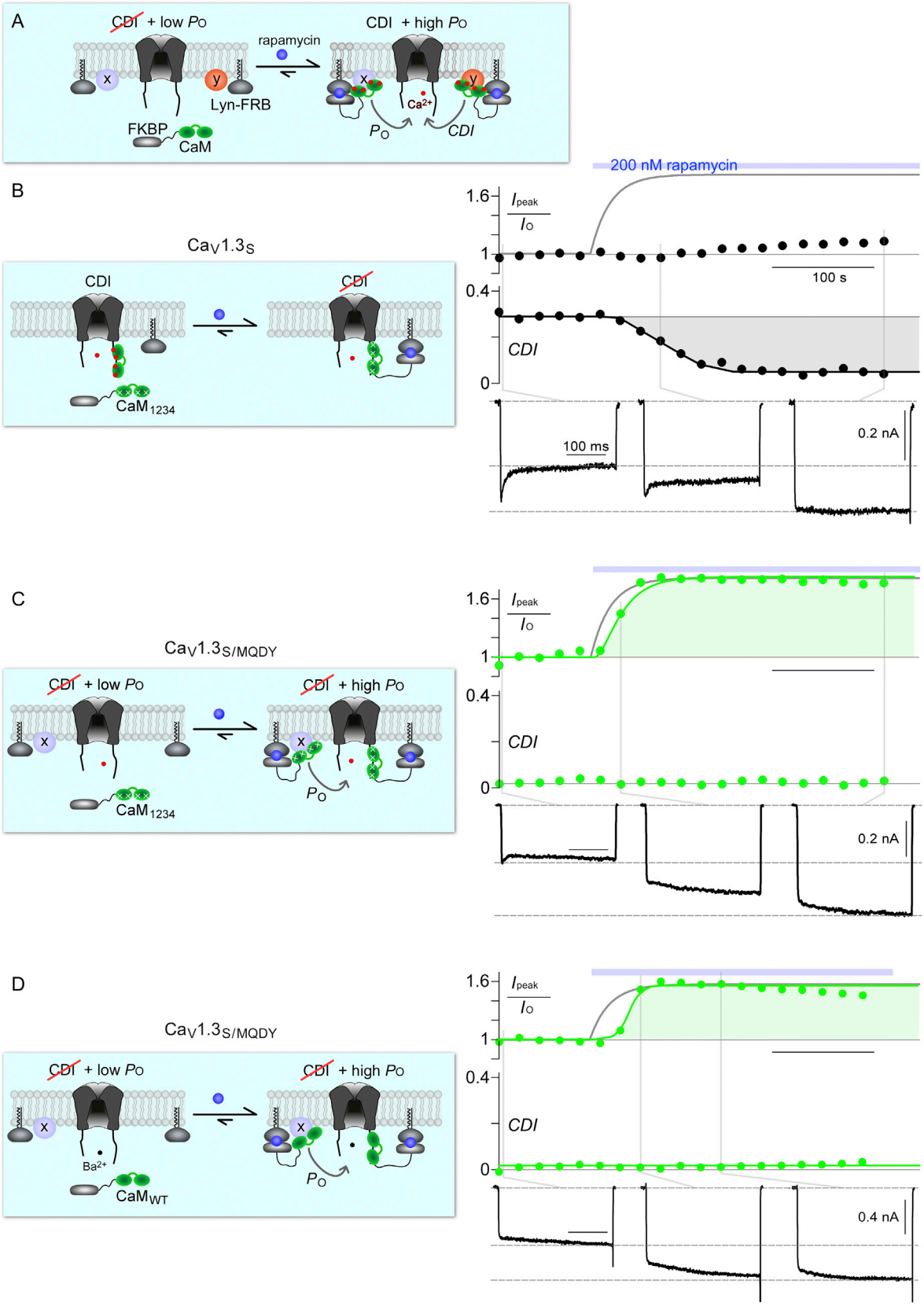

(legend on next page)

Figure S6. FRB-FKBP CaM_{1234} and Ba^{2+} Controls, Related to Figure 4

(A) Recruitment of CaM need not necessarily act via the simplest, direct-binding-to-channel mechanism outlined in main-text Figure 4A. It could be rather that P_O and CDI are modulated by the recruited CaM, but via actions through intermediary signaling molecules like Ca^{2+}/CaM-dependent kinases or phosphatases that are membrane localized near the channels (shown as x and y). Furthermore, increased P_O (I_{peak}) during CaM recruitment could be through Ca^{2+}-CaM rather than apoCaM as proposed in main text.

(B) To test direct binding of recruited CaM, we focus on the CDI limb of the overall modulatory behavior by using the $Ca_V1.3_S$ construct, which does not have appreciable change in P_O in response to CaM recruitment (see main-text Figure 4C). Here, instead of wild-type CaM, we recruit a dominant-negative mutant CaM (CaM_{1234}) to potentially eliminate CDI. Importantly, CaM_{1234} blunts inactivation via direct binding to channels in an "apoCaM" form (Mori et al., 2004; Yang et al., 2014). No Ca^{2+}/CaM recruitment is possible in this mode. As such, if the recruited CaM acts via direct binding of an apoCaM to the channel to modulate CDI, then CaM_{1234} recruitment should eliminate CDI, as depicted in left subpanel. In fact, data shown at right reveals an utter and complete elimination of CDI by recruited CaM_{1234}. Thus, for the CDI limb, recruited CaM directly binds the channel to modulate CDI. Another important implication of this experiment is that CaM_{1234} functions about like endogenous wild-type CaM to boost channel opening upon binding, as follows. This experiment concerns $Ca_V1.3_S$, which exhibits a high affinity for apoCaM such that nearly all such channels would be bound to endogenous apoCaM or recombinant CaM_{1234} throughout the experiment. Before rapamycin, the peak current (e.g., the leftmost exemplar trace) would thus be given by:

$$I_{\text{peak/before rapamycin}} = N \cdot i \cdot \left(f_{\text{before}} \cdot P_{\text{A/CaM1234}} + (1 - f_{\text{before}}) \cdot P_{\text{A/CaMendogeneous}}\right)$$
$$= N \cdot i \cdot \left(P_{\text{A/CaMendogeneous}} + f_{\text{before}} \cdot \left(P_{\text{A/CaM1234}} - P_{\text{A/CaMendogeneous}}\right)\right),$$

where N is the number of channels in the corresponding cell, i is the unitary current at the step potential, f_{before} is the fraction of channels bound to CaM_{1234} versus endogenous CaM before rapamycin, $P_{A/CaMendogeneous}$ is the open probability of channels in configuration A with endogenous CaM bound, and $P_{A/CaM1234}$ is the open probability of channels in configuration A with recombinant CaM_{1234} bound. One key here is that the fraction of channel bound to CaM_{1234} increases upon rapamycin application (to a factor $f_{after} > f_{before}$), as clearly seen from the decrease in CDI apparent in the rightmost exemplar trace. Notably, the peak current observed after rapamycin application would be given by an analogous equation:

$$I_{\text{peak/after rapamycin}} = N \cdot i \cdot \left(P_{\text{A/CaMendogeneous}} + f_{\text{after}} \cdot \left(P_{\text{A/CaM1234}} - P_{\text{A/CaMendogeneous}}\right)\right).$$

The mechanistic lesson now comes from the observation that the peak current after rapamycin ($I_{peak/after\ rapamycin}$) is essentially the same as before rapamycin ($I_{peak/before\ rapamycin}$), as seen by comparison of the amplitudes of the leftmost and rightmost exemplar currents. There is only way for the above two equations to be equal, so as to be consistent with this empirical outcome. It must be that $P_{A/CaM1234} \sim P_{A/CaMendogeneous}$. Thus, CaM_{1234} functions about like endogenous wild-type CaM to boost channel opening upon binding.

(C) What about the actions of recruited CaM on P_O? Is the Ca^{2+}/CaM form required to somehow signal to channels to increase P_O? Or, is it apoCaM binding to an intermediate signaling molecule (or the channel itself) that produces the P_O change? To investigate this, we chose to study the $Ca_V1.3_{S/MQDY}$ variant, for which recruited CaM induces not only a CDI effect, but also a P_O effect (main text Figure 4D). By recruiting CaM_{1234} to the membrane, an increase in P_O would only occur if recruited apoCaM drives the P_O effect (cartooned in left subpanel). By contrast, if recruitment of Ca^{2+}/CaM is necessary, then this experiment should produce no increase in P_O. Data at right shows a robust increase in current upon recruitment of CaM_{1234} to the membrane. Thus, recruitment of apoCaM to the membrane drives the P_O effect. A remaining ambiguity at this point is that apoCaM could bind to a factor x outside the channel, rather than to a site on the channel itself. In the simplest case, binding of one and the same CaM to the channel would mediate both CDI and P_O effects, as will be argued in main text Figure 5.

(D) To further confirm that wild-type apoCaM alone can drive the P_O effect, we performed an experiment using Ba^{2+} as the charge carrier through $Ca_V1.3_{S/MQDY}$ channels. Since CaM binds poorly to Ba^{2+}, CDI cannot be engaged. As such, recruitment of wild-type CaM to the membrane should only produce an enhancement of P_O, measured by an increase in peak current (cartooned in left subpanel). In fact, upon recruitment of wild-type CaM to the membrane, peak Ba^{2+} currents are enhanced, and no CDI is detectable (right subpanel).

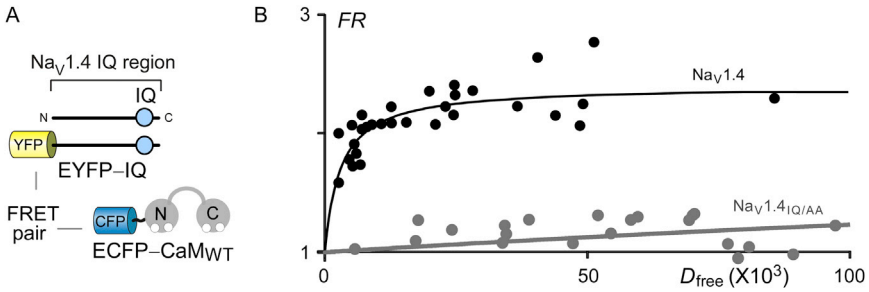

Figure S7. Na$_V$1.4 apoCaM Binding, Related to Figure 7

(A) Cartoon of FRET pairs. Na$_V$1.4 wild-type IQ, or IQ/AA peptide fused to YFP used as FRET pair with CFP-tagged wild-type CaM.

(B) FRET efficiency (*FR*) between IQ peptide and CaM is plotted versus D_{free} for Na$_V$1.4 wild-type IQ peptide (black circles) and Na$_V$1.4 IQ/AA peptide (gray circles). D_{free} is proportional to the free concentration of donor tagged molecules (i.e., CFP-CaM), where 30670 D_{free} is approximately equal to 1 μM (Bazzazi et al., 2013; Erickson et al., 2003).